Oxygen insertion reactions within the 1-D channels of phases related to $FeSb_2O_4$.

Benjamin P. de Laune,[#] Gregory J. Rees,[§] Mariana J. Whitaker,[#] Hien-Yoong Hah[a,@], Charles E. Johnson[a], Jacqueline A. Johnson[a,@], Dennis E. Brown[%], Matthew G. Tucker,[‡] Thomas C. Hansen[†], Frank J. Berry,[#] John V. Hanna,[§] Colin Greaves[#,*]

[#] *School of Chemistry, University of Birmingham, Birmingham B15 2TT, UK*
[§] *Department of Physics, University of Warwick, Coventry CV4 7AL, UK*
[a] *Center for Laser Applications, University of Tennessee Space Institute, Tullahoma, TN 37388, USA*
[@] *Department of Mechanical, Aeronautical and Biomedical Engineering, University of Tennessee Space Institute, Tullahoma, TN 37388, USA*
[%] *Department of Physics, Northern Illinois University, DeKalb, IL 60115, USA*
[‡] *Oak Ridge National Laboratory, Oak Ridge, TN 37831, USA.*
[†] *Institut Laue Langevin, BP 156, F-38042 Grenoble 9, France.*

*Corresponding author:

Prof C Greaves
School of Chemistry
University of Birmingham
Birmingham B15 2TT
UK

Email: c.greaves@bham.ac.uk

Author email:

BP de Laune	bendelaune83@gmail.com
GJ Rees	g.j.rees@warwick.ac.uk
MJ Whitaker	mjw569@gmail.com
H-Y Hah	hhah@utsi.edu
CE Johnson	cjohnson@utsi.edu
JA Johnson	jjohnson@utsi.edu
DE Brown	debrown.niu.edu@gmail.com
MG Tucker	tuckermg@ornl.gov
TC Hansen	hansen@ill.fr
FJ Berry	berryfjz@bham.ac.uk
JV Hanna	j.v.hanna@warwick.ac.uk
C Greaves	c.greaves@bham.ac.uk

Abstract

The structure of the mineral schafarzikite, $FeSb_2O_4$, has one-dimensional channels with walls comprising Sb^{3+} cations; the channels are separated by edge-linked FeO_6 octahedra that form infinite chains parallel to the channels. Although this structure provides interest with respect to the magnetic and electrical properties associated with the chains and the possibility of chemistry that could occur within the channels, materials in this structural class have received very little attention. Here we show, for the first time, that heating selected phases in oxygen-rich atmospheres can result in relatively large oxygen uptakes (up to ~2% by mass) at low temperatures (*ca* 350°C) whilst retaining the parent structure. Using a variety of structural and spectroscopic techniques, it is shown that oxygen is inserted into the channels to provide a structure with potential to show high one-dimensional oxide ion conductivity. This is the first report of oxygen-excess phases derived from this structure. The oxygen insertion is accompanied not only by oxidation of Fe^{2+} to Fe^{3+} within the octahedral chains but also Sb^{3+} to Sb^{5+} in the channel walls. The formation of a defect cluster comprising one 5-coordinate Sb^{5+} ion (which is very rare in an oxide environment), two interstitial O^{2-} ions and two 4-coordinate Sb^{3+} ions is suggested and is consistent with all experimental observations. To the best of our knowledge, this is the first example of an oxidation process where the local energetics of the product dictate that simultaneous oxidation of two different cations must occur. This reaction, together with the wide range of cation substitutions that are possible on the transition metal sites, presents opportunities to explore the schafarzikite structure more extensively for a range of catalytic and electrocatalytic applications.

1. Introduction

The tetragonal mineral schafarzikite ($FeSb_2O_4$; $P4_2/mbc$ a = 8.62 Å c = 5.91 Å)[1] is of significant interest because of its unusual 1-D structural characteristics and its ability to display a high degree of compositional flexibility. The structure is related to that of rutile, TiO_2, but neighbouring chains of edge-shared transition metal octahedra, MO_6, along [001] are now separated: in contrast to the rutile structure, the chains do not share anions with adjacent chains but are connected through O–Sb–O linkages (Figure 1). In $FeSb_2O_4$, the chains of octahedra contain Fe^{2+} (A-site), and Sb^{3+} (B-site) provides the link. The B-site has trigonal pyramidal coordination, SbO_3, which can also be regarded as *pseudo*-tetrahedral, SbO_3E, by including the stereochemically active lone pair of electrons (E). These electron pairs appear crucial for stabilizing the second key structural feature: channels that exist along [001], parallel to the chains of octahedra. Sb^{3+} ions form the channel walls and their lone pairs, E, are directed into the channels.

The structure can accommodate a range of cations on both the A-site,[2-7] and B-site.[8-10] Partial substitution of aliovalent cations at the B-site in MSb_2O_4, *e.g.* Pb^{2+} for Sb^{3+}, has previously been examined with the expectation that oxidation of M^{2+} to M^{3+} will provide charge balance and allow control over electronic and magnetic properties. Although this strategy may result in simultaneous or preferential oxidation of Sb^{3+}, resulting in mixed phase products,[11,12] we have recently achieved complete success for M = Fe, where controlled oxidation of Fe^{2+} to Fe^{3+} has been achieved.[13]

Examination of the physical properties of materials related to $FeSb_2O_4$ has, to date, been largely limited to the magnetic properties of phases containing transition metal ions,[7,12-15] for which the link between composition, structure and magnetic order is now well understood.[7,14]

A complex interplay between three magnetic exchange pathways determines the magnetic ground state: intrachain direct M-M exchange, 90° superexchange along a chain and a weaker but significant interchain M-O-Sb-O-M exchange. All systems are antiferromagnetic except for $CuAs_2O_4$ which is ferromagnetic at low temperatures.[16] The chemical reactivity of the materials has received even less attention. This is surprising since the structural channels display a feature which, to the best of our knowledge, is unique: cations (Sb^{3+} ions) form the channel walls whereas channels in oxide materials normally have walls of O^{2-} ions such that the cavities are suitable hosts for cationic species. Channel walls in aluminosilicates, for example, are O^{2-} ions from Al/SiO_4 tetrahedra. In schafarzikites, therefore, we could anticipate the chemical insertion of anions rather than cations, and here we demonstrate the first example of such a reaction, where a unique oxidation mechanism occurs for phases with A-sites containing some Fe^{2+} ions and B-sites containing some Sb^{3+} ions. Oxygen insertion into the channels occurs at low temperatures (for solid state reactions) to provide new metastable phases in which simultaneous oxidation of both Fe^{2+} and Sb^{3+} has occurred; the proposed mechanism provides suitable chemical environments for both the Sb^{3+} and Sb^{5+} cations that bond to the interstitial O^{2-} ions.

The low-temperature oxidation mechanism discussed here is thought to be unique and suggests high oxygen and/or oxide ion mobility within the channels. It is pertinent to note that low-dimensional structures containing partially filled oxide ion sites have recently gained interest for energy materials since they can provide an interstitialcy mechanism for oxide ion migration rather than the normal vacancy driven mechanism that occurs, for example, in the fluorite solid electrolyte YSZ, $Zr_{1-x}Y_xO_{2-x/2}$.[17] This interest also extends to cathode materials where mixed conductivity is required. A recent example is the study of the oxygen excess, mixed conducting, Ruddlesden−Popper phases $(La,Pr)_2(Ni,Co)O_{4+\delta}$[18] where the excess

oxygen enters the structure between two adjacent rocksalt-related layers and can coordinate tetrahedrally to lanthanide ions. In this respect, materials with channels containing highly mobile interstitial oxide ions would be of especial interest. Given that a range of transition metals can occupy the chains of octahedra, the focus of this study is therefore also highly relevant to the search for new catalysts and electrocatalysts.

2. Experimental

A variety of compounds with the schafarzikite structure were synthesised by heating intimately ground stoichiometric mixtures of dried metal oxides and metals in evacuated, sealed quartz tubes at 600-750°C for 6 hr periods with intermittent grinding. Alumina inserts were used to prevent reaction with the quartz. Critical to the results presented in this paper is the amount of Fe^{2+} per formula unit (pfu); this was controlled by either isovalent cation substitutions at the A-site or aliovalent substitution of Pb^{2+} for Sb^{3+} at the B-site, and compositions with particular relevance to this paper are given in Table 1. The compositions reported here were chosen to provide important control of the Fe^{2+} content (given in Table 1); this was kept quite low to avoid large oxygen absorption, which was found to result in broadened diffraction peaks. Both Mg^{2+} and Co^{2+} substitutions for Fe^{2+} were used to provide substantial differences to electronic conductivity within the chains of octahedra. The partial substitution of Pb^{2+} for Sb^{3+} not only reduced the Fe^{2+} content but also enhanced the high temperature stability which was important for revealing that the oxidation involved two discrete steps. Oxidised phases were created by heating samples in air or oxygen. For ^{17}O NMR analysis, samples of $MgSb_2O_4$ and Sb_2O_3 were exchanged with ^{17}O-enriched H_2O hydrothermally and $FeSb_2O_4$-related phases were exchanged with ^{17}O-enriched oxygen gas (75% enrichment) at 350°C for times of 12-66 min. depending on the observed rate of oxygen absorption. Full experimental details are provided in Supplementary Information.

3. Results

3.1 Thermogravimetric analysis (TGA).

Mass changes for three representative samples heated in oxygen gas are shown in Figure 2. All are unstable above 600°C and form Sb^{5+}-containing products; $CoSb_2O_4$, for example, simply forms $CoSb_2O_6$ with a mass increase of *ca* 8% (expected 8.7%). However, a low-temperature plateau is also observed centred at ~ 400°C for ***all*** samples containing Fe^{2+} ions. Indeed, the sample $Co_{0.25}Fe_{0.75}Sb_{1.75}Pb_{0.25}O_4$ shows strong evidence that an additional process occurs at higher temperatures to provide a second plateau centred at ~ 550°C. It should be emphasized that the low-temperature plateau is not observed for $CoSb_2O_4$ and is observed *only* in samples containing Fe^{2+}; moreover, the mass increase at this plateau is related to the amount of Fe^{2+} in the sample (see Figure 3). It is assumed that for all materials investigated, the substitution of Pb^{2+} for Sb^{3+} is balanced only by oxidation of Fe^{2+} to Fe^{3+} in accordance with previous studies.[13] The clear link between the mass increase and the Fe^{2+} content of the sample may, at first sight, suggest that for every O^{2-} ion absorbed, charge balance is satisfied by oxidation of $2Fe^{2+}$ to $2Fe^{3+}$. However, a critical feature for all samples exhibiting the low temperature plateau is that the amount of oxygen absorbed is, in fact, significantly *higher* than that expected for oxidation of all Fe^{2+} to Fe^{3+}. This is clear in Figure 3 which also shows that the oxygen uptake at low Fe^{2+} contents (up to $0.50Fe^{2+}$ pfu) is, in fact, approximately twice that expected. Two possibilities were considered as plausible explanations: either other cations, in addition to Fe^{2+}, are oxidised (or higher oxidation states of Fe are formed), or oxygen enters as peroxide ions, O_2^{2-}, rather than O^{2-} ions. A structural study was therefore conducted to determine the precise nature of the structural changes that occur during oxidation.

3.2 The structure of $FeSb_{1.25}Pb_{0.75}O_{4+y}$

XRPD analysis of samples obtained by cooling from the low temperature plateaus on the TGA plots revealed that the basic structure had been retained (space group $P4_2/mbc$) but with changes to the unit cell dimensions: a reduction in *a* and increase in *c*. This is similar to that observed when Pb^{2+} is substituted for Sb^{3+} in $FeSb_2O_4$, where oxidation of A-site cations within the chains of octahedra results in increased intrachain Fe–Fe repulsions and consequently an expansion of *c*. For samples with large Fe^{2+} contents, *e.g.* $FeSb_2O_4$, the large amount of oxygen incorporation resulted in a degree of structure degradation; structure determination was therefore focused on the oxidation product of $FeSb_{1.25}Pb_{0.75}O_4$, which initially contained 25% Fe^{2+} and 75% Fe^{3+}.[13] Figure 3 shows that a significant oxygen uptake occurs for this composition and a sample for NPD study (~4 g) was prepared by heating in air at 400°C for 12 min. TGA suggested that the final composition was $FeSb_{1.25}Pb_{0.75}O_{4.29(1)}$ compared to $FeSb_{1.75}Pb_{0.25}O_{4.125}$, which is predicted if oxygen insertion as O^{2-} ions is balanced only by oxidation of Fe^{2+} to Fe^{3+}.

NPD data (HRPT at PSI, 300 K, λ = 1.8852 Å) were collected on $FeSb_{1.25}Pb_{0.75}O_{4.29(1)}$ at ambient temperature. Because of the relatively small change in composition, structure refinement based on the structure of the stoichiometric, unoxidised material gave a good fit to the data. However, Difference Fourier maps suggested additional scattering density within the channels, as shown in Figure 4; inclusion of an oxide ion into the refinement at the suggested position resulted in a small, but statistically significant, improvement to the fit (χ^2 decreased from 2.6 to 2.2). The profiles for the refinement are given in Figure 5 and the refined structural parameters are given in Table 2 where O3 represents the incorporated interstitial oxygen, O1 the apical and O2 the equatorial positions (see Figure 1). The disorder, from both the mixed Sb/Pb on the 8*h*-site and the interstitial oxygen, resulted in high displacement parameters and significantly anisotropic displacement parameters for O1. The

Sb/Pb site occupancy was constrained to that weighed out. The refined composition, $FeSb_{1.25}Pb_{0.75}O_{4.24(1)}$ is in good agreement with the TGA value of $FeSb_{1.25}Pb_{0.75}O_{4.29(1)}$. The refined structure is shown in Figure 6, and some bond distances and bond valence sums (BVS)[19] are given in Table 3. The shortest O3–O3 distances are 1.09(3) Å and 1.54(5) Å, the latter being across the centre of the channel as shown in Figure 6. Although these distances are too short for fully occupied sites, it should be noted that only 6% of the 16*i*-sites are actually occupied so the model is entirely satisfactory for such an average structure. Table 3 gives the BVS for Fe (2.91) based on the r_o parameter for Fe^{3+}, 1.759.[19] This methodology has previously been found to yield excellent agreement between the Fe BVS and the Fe oxidation state for $FeSb_{1-x}Pb_xO_4$ with $x > 0.4$.[13] For the Fe oxidation states of 2.45+, 2.50+ and 2.70+, the bond distances in reference 13 give BVS values of 2.54, 2.54 and 2.64. The BVS of 2.91 (Table 3) therefore provides strong evidence that the oxygen incorporation has resulted in complete oxidation of the Fe^{2+} present to Fe^{3+}. However, the increase in oxygen content determined by the O3 occupancy is approximately twice that expected for a model in which insertion of O^{2-} ions is accompanied by oxidation of all Fe^{2+} to Fe^{3+}. The O3–O3 separation of 1.54 Å across the centre of the channel is therefore of particular interest since it is similar to the O–O separation in simple peroxides, *e.g.*1.49 Å in Na_2O_2.[20] The existence of peroxide (or even superoxide) links within the structure could explain why the observed mass increase is higher than that expected for simple oxidation of Fe^{2+} to Fe^{3+}. A possible O–O linkage is marked in Figure 6, where the O3 species are bonded to Sb/Pb at a distance of 1.91(4) Å (Table 3).

3.3 Structural changes during oxidation.

In order to obtain more detailed information on the structural changes occurring during the oxidation, and hence the mechanism involved, an *in situ* NPD study was conducted (D20 at

ILL, Grenoble, λ = 1.5430 Å). The sample chosen for investigation was $Co_{0.25}Fe_{0.75}Sb_{1.75}Pb_{0.25}O_4$ since it has a high final decomposition temperature and a double plateau at low temperatures (Figure 2). Essential experimental details are given in ESI for the oxidation under flowing oxygen with structural data collected up to 500°C. Initially, data were collected for 5 min (5°C) intervals up to 350°C, conditions which were expected to yield a composition on the first low temperature plateau. Data were then collected for several extended periods (15 min) at 350°C before temperature ramping was continued up to 500°C. To minimise the effects of correlation between the O3 site occupancy and its isotropic displacement parameter (IDP), the IDPs for O1, O2, and O3 were constrained to be equal; in addition, Fe/Co site occupancy was constrained to 0.75/0.25, *i.e.* as weighed out. Typical raw neutron diffraction data (corresponding to 320°C) are shown in Figure 7(a) and (b), and the profiles corresponding to the final refinement for this temperature are shown in Figure 7(c). Changes to important structural parameters are shown in Figure 8.

Occupancy of the interstitial oxygen site, O3, increased with temperature (T) primarily in the range 200ºC < T < 350°C (Figure 8(a)). On reaching 350°C, the O3 occupancy corresponds to an oxygen content of 4.40(2), in good agreement with the TGA value (Figure 2) of 4.36 at the mid-point of the plateau. However, full oxidation of Fe^{2+} to Fe^{3+} can account for only 4.25 oxygen pfu. The small discontinuity in the data at 350°C is a consequence of the isothermal measurements that were taken at this temperature. Figure 8(a) shows further increase in the O3 site occupancy between 350°C and 500°C, but the slope for the uptake is reduced in this higher temperature region. It is important to note that all structural changes recorded in Figure 8 show a distinct discontinuity at approximately 350°C, which suggests a change in the oxidation mechanism at about this temperature. This was confirmed by other techniques and details are presented later (sections 3.6 and 4).

Figures 8(b) and (c) show changes to the unit cell parameters during the main oxidation (200°C < T < 350°C): *a* decreases, *c* increases and the volume decreases. This behaviour is very similar to that observed for increasing *x* in $FeSb_{2-x}Pb_xO_4$ where the increase in *c* was attributed to enhanced cation-cation repulsion within the chains of octahedra resulting from the oxidation of Fe^{2+} to Fe^{3+}.[13] For T > 350°C, some oxidation continues (Figure 8(a)) but the main changes to the unit cell appear to be thermal in nature and the volume increases with temperature. These data support the importance of oxidation of Fe^{2+} to Fe^{3+} at temperatures up to 350°C. Confirmation is provided by the decrease in the average Fe/Co – O bond distance within the octahedra, Figure 8(d). Simple bond valence sum calculations,[19] based on oxidation of all the Fe^{2+} present to Fe^{3+}, show that the changes observed are compatible with such a process. Since no low-temperature oxidation of $CoSb_2O_4$ occurs, Figure 2, we conclude that facile oxidation of Co^{2+} does not occur.

Figures 8(e) and (f) show data with direct relevance to oxygen entering the channels. The change in distance between two Sb/Pb cations immediately across a given channel is seen in Figure 8(e) and shows a substantial decrease of 7% (from 4.00 Å to 3.73 Å); this is largely responsible for the contraction in the unit cell *a* parameter (Figure 8(b)). The decrease in channel diameter is also consistent with the insertion of negative O^{2-} ions which can bond to the positive ions that form the channel walls, in this case Sb^{3+} and Pb^{2+}. Since oxidation of Pb-free schafarzikites display the same oxidation characteristics, lead cannot be actively involved in the oxidation mechanism, and the formation of Sb – O bonds must occur. This bond formation is consistent with the change in the average bond length for the three Sb/Pb – O1/O2 bonds, Figure 8(f). In marked contrast to the Fe/Co – O distances (Figure 8(d)), these bonds increase with the level of oxidation and cannot simply relate to oxidation of Sb^{3+} to

Sb^{5+}. Although BVS estimates are not straightforward because of the partial substitution of Pb on the Sb sites, Figure 8(f) shows the predicted average bond distances derived from BVS calculations for this site when coordinated to both 3 and 4 oxygens. The calculations are weighted to include the contribution from Pb^{2+} ions. The figure supports the hypothesis that oxygen enters the channels and bonds to Sb to form 4-coordinate Sb^{3+}. However, it must be remembered that not all Sb^{3+} ions will be bonded to an extra O^{2-} ion, so the apparent quantitative agreement of the data in Figure 8(f) is partly coincidental.

The *in situ* structural examination gives significant information concerning the nature of the oxidation of $Co_{0.25}Fe_{0.75}Sb_{1.75}Pb_{0.25}O_4$ and hence other related phases. It is clear that oxidation of cations within the chains of octahedra occurs, but the level of interstitial oxygen is higher than this mechanism can support; in this respect, the data endorse the results from TGA analysis. At this stage, two mechanisms remained plausible to explain the enhanced oxygen content for the materials oxidised without phase decomposition:

i. Peroxide links occur across the channels, *e.g.* Sb – O – O – Sb as shown in Figure 6;
ii. Another oxidation process accompanies the oxidation of Fe^{2+} to Fe^{3+}.

In order to resolve this uncertainty, additional information was sought from Raman spectroscopy, neutron PDF analysis, Mössbauer spectroscopy, NMR spectroscopy and X-ray photoelectron spectroscopy (XPS); the results are discussed below and in Supplementary Information.

3.4 Raman spectroscopy.

The best method to probe the existence of – O – O – bonds is Raman spectroscopy for which the O – O vibration is characterised by a band in the Raman shift range 750 – 850 cm^{-1}.[21] The parent material, $FeSb_2O_4$, has previously been studied and the strongest band at 668 cm^{-1}

was assigned to a Sb – O vibration with symmetry A_{2g}.[22] We have examined a range of materials oxidised by heating in oxygen as previously described (*vide supra*) but have not found any evidence for a vibrational band to support the presence of peroxide (or superoxide). Figure 9, for example, shows spectra for $Co_{0.75}Fe_{0.25}Sb_2O_4$ before and after oxidation. The spectrum of the initial material agrees well with that previously described for $FeSb_2O_4$,[22] whereas the oxidised material has broadened bands which often show shoulders. The principal Sb – O vibration shows such features which are to be expected because of the change in coordination of some of the Sb^{3+} ions following oxidation. However, no band in the O_2^{2-} region (or at higher shifts compatible with O_2^-) is seen which precludes the existence of such species in the oxidised compounds.

3.5 Neutron PDF analysis

In this report, we focus only on the small separation distance (*r*), *i.e.* the region around 1.5 Å in the PDF data (Figure 10), where we would expect to see intensity originating from any peroxide species present. Comparison of the intensities between the oxidised and parent phases in this region reveals no increase in intensity caused by the insertion of interstitial oxygen. Unfortunately, this region coincides with the truncation ripples produced when performing the Fourier transform of the data into real space which will inherently limit the sensitivity of the PDF data in this region. However, the decrease in the intensity of the oxidised phase relative to the parent material supports the absence of peroxide species. More detailed analysis of these data is currently in progress to examine other structural changes, *eg* coordination of the Sb ions, and will be reported separately.

3.6 Mössbauer spectroscopy

Since no low-temperature oxidation of $CoSb_2O_4$ occurs, Figure 2, Co^{2+} oxidation cannot occur under the low temperature oxidation conditions employed. The preferential oxidation of Sb^{3+} rather than Co^{2+} is supported by the formation of the trirutile $CoSb_2O_6$ (containing Co^{2+} and Sb^{5+}).[23] Similarly, the synthesis of $FePbBiO_4$ (containing Fe^{3+} and Pb^{2+} ions)[24] and $Pb_2Sb_2O_7$ (containing Sb^{5+} and Pb^{2+} ions)[25] under oxidising conditions illustrates that Pb^{2+} ions are thermodynamically stable in the presence of Fe^{3+} and Sb^{5+} ions and will also remain unoxidised in the reactions under current discussion. The formation of Fe^{4+} ions in the presence of Sb^{3+} was considered highly unlikely, and the most plausible mechanism to explain the experimental obervations was one involving the simultaneous oxidation of Fe^{2+} (to Fe^{3+}) and Sb^{3+} (to Sb^{5+}) during the low temperature oxidation reaction. Since Mössbauer spectroscopy is the most powerful probe to determine Fe and Sb oxidation states, ^{57}Fe and ^{121}Sb Mössbauer spectra were collected to test this hypothesis. Although data were collected on a variety of materials, here we focus only on $Co_{0.25}Fe_{0.75}Sb_{1.75}Pb_{0.25}O_4$ and its oxidised product for which we are able to compare results with those from the detailed *in situ* NPD data.

Figures 11 and 12 show ^{57}Fe and ^{121}Sb Mössbauer spectra for the initial compound and the sample after oxidation in air at 350°C for 3 h, respectively. It can be seen that the absorption peaks from Sb^{3+} are suggestive of more than one component, which may relate to various factors including quadrupolar effects and the presence of more than one Sb^{3+} site post-oxidation (*vide infra*). These are under investigation and will be reported later; for the present analysis, since the Fe and Sb oxidation states are of primary concern, the Sb^{3+} absorption peaks have been fitted to a single site but quadrupole splitting effects have been included. Table 4 gives the detailed Mössbauer parameters. The ^{57}Fe spectrum for the initial material, Figure 11(a), suggests 58% Fe^{2+} and 42% Fe^{3+} based on the respective peak areas (Table 4).

Correction of these ambient temperature data for Fe^{2+} and Fe^{3+} Debye-Waller factor effects (using thermal factors for $FeSb_2O_4$[13] and $FePbBiO_4$[24]), results in the composition 62% Fe^{2+} and 38% Fe^{3+}, in reasonable agreement with the values expected for an initial composition of 0.50 Fe^{2+} and 0.25 Fe^{3+}pfu (67% Fe^{2+} and 33% Fe^{3+}).

Full oxidation of Fe^{2+} to Fe^{3+} is indicated in the product of oxidation at 350°C, Figure 12(a), but no evidence for higher oxidation states of Fe have been observed; the formation of Fe^{4+} was therefore eliminated from the oxidation mechanism. The partial oxidation of Sb^{3+} to Sb^{5+} indicated in the ^{121}Sb spectrum in Figure 12(b) is therefore of major significance. The peak areas in the ^{121}Sb Mössbauer data recorded at 90 K, Table 4, are necessary to provide a reliable estimate for the Sb^{5+} concentration (18(5)%). The difference between this value and that deduced from the peak areas in the ambient temperature data (22(5)%) is expected because of the significantly higher Debye-Waller factor for the lower valent Sb^{3+} ion (compared with Sb^{5+}), and the resulting lower recoil-free fraction at 300 K for Sb^{3+} compared with Sb^{5+}. At 90 K, the recoil-free fractions for both oxidation states are similar. For 18(5)% conversion of Sb^{3+} to Sb^{5+} (Table 4) and all Fe being present as Fe^{3+}, the final composition would be $Co_{0.25}Fe_{0.75}Sb_{1.75}Pb_{0.25}O_{4.57(9)}$, which is in excellent agreement with the NPD data in Figure 8(a) which suggests an oxygen content of 4.50 pfu. The critical conclusion is that the oxidation process at 350°C does indeed relate to the oxidation of ***both*** Fe^{2+} to Fe^{3+} ***and*** Sb^{3+} to Sb^{5+}. We note that two Fe^{2+} ions (0.50 pfu) are oxidised for one Sb^{3+} (14.3% Sb corresponds to 0.25 Sb pfu) and this is discussed in detail later.

Mössbauer data were also collected for a sample heated slowly to 500°C in oxygen, held for one hour, and then slowly cooled; the results are given in Figure 13 and Table 4. As expected, the Fe^{2+} was fully oxidised to Fe^{3+} and more Sb^{3+} was oxidised to Sb^{5+} to yield a

composition of $Co_{0.25}Fe_{0.75}Sb_{1.75}Pb_{0.25}O_{4.93}$. This compares with the compositions revealed by NPD for a sample heated at 500°C but under two different overall synthetic conditions: at the end of the ramping to 500°C, the oxygen content is $O_{4.64(2)}$ (Figure 8(a)); after holding at 500°C for an hour it has risen to $O_{4.74(2)}$. These three compositions – $O_{4.64}$, $O_{4.74}$ and $O_{4.93}$ – correspond to samples approximately at the beginning, middle and end of the higher temperature plateau shown in Figure 2 and the differences in composition can be attributed to kinetic factors. The Mössbauer data are therefore strongly supportive of a two-step low-temperature oxidation process (*i.e.* prior to full oxidation at temperatures > ~600°C). These steps are reflected in the two low-temperature plateau regions that occur in the TGA plots (Figure 2) and the difference in structural trends that are observed in the *in situ* NPD data below and above 350°C (Figure 8) and discussed in section 3.3. The oxidation processes relate to synchronous oxidation of Fe^{2+} to Fe^{3+} and Sb^{3+} to Sb^{5+} below ~350°C (until all Fe^{2+} is oxidised), and subsequent further oxidation of Sb^{3+} to Sb^{5+} at higher temperatures.

3.7 ^{17}O NMR spectroscopy.

In order to obtain additional information concerning the nature of oxygen absorption, especially with respect to possible peroxide formation, ^{17}O NMR spectra were recorded for Fe^{2+}-containing samples after oxidation in ^{17}O-enriched oxygen gas. To assist the interpretation of the spectra, the ^{17}O and ^{25}Mg MAS NMR data of the diamagnetic $MgSb_2O_4$ and Sb_2O_3 systems were also obtained and are shown in Figure 14; the measured NMR parameters and the associated GIPAW DFT calculated parameters are summarised in Table 5. The variable B_0 field ^{17}O MAS NMR data of Figure 14(a) shows the presence of two resonances associated with the apical and equatorial positions in the $MgSb_2O_4$ lattice; these are denoted as sites 1 and 2, respectively, and correspond to O1 and O2 in Figure 1 and Tables 2 and 3. In addition, channel H_2O and surface OH^- species are observed. The presence

of all four O species is corroborated by the ^{17}O 2D 3QMAS data of Figure 14(b). A comparison of the δ_{iso} and P_Q values elucidated from the variable B_0 field analysis of the data characterising sites 1 and 2 (see Figure 14(c)) with the corresponding calculated GIPAW DFT values demonstrates that only one of the O positions exhibits a good agreement between measurement and calculation. Furthermore, the ^{25}Mg δ_{iso}, P_Q, C_Q and η parameters measured from the data of Figure 14(d) are in excellent agreement with the GIPAW DFT calculated values, especially after geometry optimisation. Hence, it can be inferred that the residual H_2O and OH^- speciation in the channels selectively influence only one of the framework O positions. Similar evidence of this selective influence emanates from the ^{17}O MAS NMR data from Sb_2O_3 shown in Figure 14(e); although the apical and equatorial O positions of $MgSb_2O_4$ are comparable, possessing similar arrangements with the Sb positions, only the apical site 1 exhibits δ_{iso}, C_Q and η values that are in agreement with the Sb_2O_3 unit thus suggesting that the interaction with channel H_2O and surface OH^- species influences the equatorial site 2 represented by the upfield resonance.

Solid state ^{17}O NMR studies on paramagnetic materials are uncommon due to O typically being directly bonded (or in close spatial proximity) to paramagnetic species.[30] The ^{17}O MAS NMR data of the paramagnetic schafarzikite-related systems shown in Figure 15 are hyperfine shifted, presumably by contributions from both the pseudo-contact shift and the Fermi contact interactions. These spectra exhibit broad characteristic anisotropies which are represented as manifolds of spinning sidebands that are usually associated with the pseudo-contact shift contribution. Through the implementation of variable MAS frequencies the isotropic position of each sideband manifold has been determined. It is proposed that the narrow ^{17}O resonances at δ_{iso} ~2150 and ~1850 ppm represent the high symmetry axial and equatorial oxygen environments of the framework which corroborates the NPD results. A

substantial amount of labelled O is located in the channels and is responsible for the broad underlying component (span $\Delta\delta$ ~0 - 4,000 ppm) that resides underneath the better defined spinning sideband manifolds (see Figures 15(b)-(e)). This observation is also supported by the NPD refinement, with the broad nature of this resonance indicating a clear lack of order in these channel O environments. A direct comparison of the ^{17}O MAS NMR data measured from diamagnetic $MgSb_2O_4$ (see Figure 15(a)) with the paramagnetic schafarzikite-related systems shown in Figures 15(b)-(e) indicates that the magnitude of the paramagnetic shifts and anisotropies are dependent on the nominal composition and the relative amounts of the paramagnetic Co^{2+}, Fe^{2+} and Fe^{3+}defining each system.

The NMR data therefore show significant ^{17}O substitution at the lattice O1 (apical) and O2 (equatorial) sites following short oxygen incorporation reactions. This indicates that oxide ion diffusion is occurring within the structural framework in addition to that within the channels. The broad signals from the channel sites prevent definitive characteristion of their environment, but do not support the presence of peroxide bond formation.

3.8 Electronic conductivity

Conductivity data were collected on pellets of $Co_{0.50}Fe_{0.50}Sb_2O_4$ under three conditions: ramping up to 500°C in dry nitrogen; ramping up to 500°C in air and then cooling; ramping to 350°C under dry nitrogen and then switching the atmosphere to dry oxygen under isothermal conditions. The results are shown in Figure 16. Figure 16(a) shows, in blue, the variation of the conductivity of the starting material with temperature (the heating is in nitrogen gas). The black lines/symbols shows the major effects of heating in air: the oxidation begins at *ca* 260°C and results in an increase in conductivity; the conductivity peaks at 330°C and then falls to a value below that of the starting material heated in nitrogen. This behaviour reflects the increased electronic conductivity caused by the presence of both

Fe^{2+} and Fe^{3+} ions and was seen previously for the system $FeSb_{2-x}Pb_xO_4$,[13] where the conductivity was highest for equal Fe^{2+} and Fe^{3+} concentrations. The same data plotted as log(conductivity) against 1000/T are shown in Figure 16(b) where the red lines are linear fits to the data prior to oxidation and on cooling of the oxidized product. The good fits indicate thermally promoted conduction with activation energies of 19.5(2) kJ mol^{-1} and 21.3(2) kJ mol^{-1} for the unoxidised and oxidised materials, respectively. The conductivity for $Co_{0.50}Fe_{0.50}Sb_2O_4$ is approximately an order of magnitude lower than that reported for $FeSb_2O_4$,[13] which suggests that electron migration primarily involves Fe^{2+}. Figure 16(b) shows that the conductivity of the oxidized phase, $Co_{0.50}Fe_{0.50}Sb_2O_{4+y}$, is lower than that for $Co_{0.50}Fe_{0.50}Sb_2O_4$ by a factor of about 5. Since the conduction will be dominated by the chains of octahedral transition metals, this is probably linked to the expansion along [001], the chain direction, during oxidation and the resulting effect on Fe – Fe separation. It should be noted that the small discrepancy between the measurement in nitrogen and the low temperature measurement in air can be traced to a significant difference in pellet densities: 50% for the pellet in air *cf* 77% for the pellet in nitrogen.

Figure 16(c) reports data for subsequent isothermal oxidation at 350°C of the pellet that had previously been heated in nitrogen to provide the data (in blue) shown in Figures 16(a) and 16(b). The data are recorded against time after the gas was switched from nitrogen to oxygen. After an initial delay corresponding to gas diffusion in the system, virtually complete pellet oxidation is achieved after approximately 7 min. This rapid reaction suggests the likelihood of high oxide ion mobility for the interstitial ions within the channels of these materials.

4. Discussion

The NPD and TGA data clearly indicate that low-temperature oxidation of schafarzikite materials that contain both Fe^{2+} and Sb^{3+} is associated with oxygen entering the channels and bonding to Sb^{3+} ions. However, the level of oxygen incorporation is greater than that corresponding to oxidation of Fe^{2+} to Fe^{3+} within the octahedral chains. Moreover, the data consistently suggest that for Fe^{2+} concentrations of < 0.5 pfu in the unoxidised samples, the oxygen uptake is *ca* twice that expected. Mössbauer spectra reveal that charge balance associated with the extra oxygen content is provided by oxidation of Sb^{3+} to Sb^{5+}. To examine the change in oxidation states of all four cations in $Co_{0.25}Fe_{0.75}Sb_{1.75}Pb_{0.25}O_4$, XPS data were collected but the changes observed were insufficient to resolve the details of the redox reactions. However, oxidation of neither Co^{2+} nor Pb^{2+} is plausible as discussed in Section 3.6. With respect to the formation of Sb^{5+} ions, it is relevant to note that an attempt to partially substitute Sb^{3+} by Pb^{2+} in $MnSb_2O_4$[11] resulted in oxidation of Sb^{3+} rather than the desired Mn^{2+}, and the resulting Sb^{5+} ions entered the octahedral sites by replacing some of the Mn^{2+} ions. This possibility was rejected for the oxidations studied here for two reasons: 1) substitution of Sb^{5+} ions in the chains of octahedra would result in significant impurity phases; 2) XRPD and NPD are both sensitive to such mixing and both confirm that no detectable substitution of Sb within the chains occurs. The Sb^{5+} ions therefore remain on the channel walls and it is therefore important to consider how the insertion of oxygen ions into the O3 sites can satisfy the very different stereochemical preferences of Sb^{3+} and Sb^{5+} ions.

For the oxidation of $Co_{0.25}Fe_{0.75}Sb_{1.75}Pb_{0.25}O_4$, the first low temperature plateau corresponds closely to oxidation of all Fe^{2+} to Fe^{3+} ($0.50Fe^{2+}$ forming $0.50Fe^{3+}$) and the simultaneous oxidation of $0.25Sb^{3+}$ to $0.25Sb^{5+}$; this would correspond to an oxygen content of 4.50 pfu which is close to that determined by TGA, NPD and Mössbauer spectroscopy. To consider the likely environment for Sb^{5+}, it is informative to explore in more detail the local

environment of the O3 site. As shown in Table 3, each O3 is close to two adjacent Sb sites with Sb – O3 distances of 1.91 and 2.30 Å. BVS considerations require an average Sb – O distance of 1.97 Å in the unoxidised phase, less than the observed value of 2.10 Å (Figure 8(f) because the larger Pb^{2+} ion occupies the same site. An additional bond at 2.30 Å would require an expansion of the three lattice bonds by 0.06 Å to 2.03 Å to retain the same BVS value. Figure 8(f) shows that this should readily be achieved and suggests that the larger Sb – O3 distance corresponds to 4-coordinate Sb^{3+}. The bond at 1.91 Å, however, would require a corresponding expansion of 0.19 Å to 2.16 Å. This appears less likely, and this bond distance is more indicative of Sb^{5+}: expected average Sb^{5+} – O distances of 1.86 Å, 1.94 Å and 2.01 Å for coordination numbers of 4, 5 and 6, respectively. It therefore seems highly likely that the Sb^{5+} ions, which we have shown to be essential to explain the observed oxygen contents, are adjacent to a 4-coordinate Sb^{3+} ion. The oxidation of Sb^{3+} to Sb^{5+} ion is accompanied by the introduction of an extra oxide ion into the structure; this can coordinate to the Sb^{5+} ion (Sb^{5+} – O bond distance of 1.91 Å) to provide a 5-coordinate species without a lone pair, and also provide a link to a second 4-coordinate Sb^{3+} ion *via* a longer bond (Sb^{3+} – O bond distance of 2.30 Å). We therefore suggest the presence of defect clusters which contain two interstitial O^{2-} ions, two 4-coordinate Sb^{3+} ions and one 5-coordinate Sb^{5+} ion. This arrangement is shown in Figure 17 and is based on the average atom coordinates given in Table 2 from the high resolution NPD data for $FeSb_{1.25}Pb_{0.75}O_{4+y}$. Figure 17 shows that the spatial coordination of O3 retains space for the lone pair on the 4-coordinate Sb^{3+} ion whose stereochemistry can be related to a trigonal bipyramid, SbO_4E, where the lone pair (E) occupies an equatorial position. Sb^{5+}, on the other hand, is 5-coordinate with a structure that can be described as either distorted square pyramidal or distorted trigonal bipyramidal. Sb^{5+} ions are normally octahedral in extended oxide structures, but a similar distorted geometry has previously been suggested in $Sr_2MSbO_{5.5}$ (M = Ca, Sr, Ba).[31] We can use the BVS model

for 3-coordinate Pb^{2+} ions (predicted Pb – O bond 2.262 Å)[19] to estimate Sb – O distances from the *average* bond distances in Table 3: Sb – O1 and Sb – O2 are reduced to 2.016 Å and 1.995 Å, respectively. This allows calculation of the BVS values: 2.78(8) for 3-coordinate Sb^{3+} (bonded to O1, O2 [×2]), 3.19(9) for 4-coordinate Sb^{3+} (bonded to O1, O2 [×2], O3 at 2.30 Å) and 4.73(14) for 5-coordinate Sb^{5+} (bonded to O1, O2 [×2], O3 [×2] at 1.91 Å). The structural model shown in Figure 17 is therefore able to satisfy the bonding requirements of both Sb^{3+} and Sb^{5+}.

Considering the oxidation of $Co_{0.25}Fe_{0.75}Sb_{1.75}Pb_{0.25}O_4$ and the structural data shown in Figure 8, the cluster discussed above can fully explain the oxidation up to 350°C, where the O3 site occupancy corresponds to an oxygen content of 4.5 pfu. At this point, oxidation of all the 0.50 Fe^{2+} in the compound provides 0.25 interstitial O, and oxidation of $0.25Sb^{3+}$ to Sb^{5+} contributes the same amount. This is fully supported by the Mössbauer spectra. However, it is clear from Figure 8 that oxidation continues at higher temperatures, albeit to a lesser extent. Although the structural data currently available do not allow a definitive answer to the nature of this process, it is noted that each of the 4-coordinate Sb^{3+} ions which terminate the cluster shown in Figure 17 could be oxidised to Sb^{5+} and be bonded to an additional O3 ion (with short Sb – O bond) which would then create a new 4-coordinate Sb^{3+} ion at the end of the chain. We would expect this chain extension to cause minor changes to the existing O3 atoms shown in Figure 17, but these would not be apparent in the structure refinements discussed here. However, the changes seen in Figure 8 for temperatures above 350°C are significant and indicate a change in mechanism for the oxidation process. This also manifests itself in Figure 2 where TGA data display a second plateau at temperatures above 350°C. The Mössbauer data collected for a sample after extended heating at 500°C, Figure 11, indicate a composition that is located on this plateau.

It is acknowledged that the formation of the proposed clusters will be restricted by the random distribution of Pb^{2+} on the Sb^{3+} sites. However, statistically the effect would be small for the materials studied here. For example, for $Co_{0.25}Fe_{0.75}Sb_{1.75}Pb_{0.25}O_4$, bonding an inserted O3 ion to a given Sb would allow further bonding to one of two possible sites that would then become Sb^{5+}. Each of the two sites has a 12.5% probability of being occupied by Pb, which corresponds to a probability of only 1.6% that they would *both* be occupied by Pb. The Sb^{5+} can then bond to only one Sb^{3+} (probability 12.5% Pb) since it can form only two bonds at 1.91 Å. Overall, the probability that the O3 ion can form the chain shown in Figure 17 is 86%. Of course, as more clusters form, the probability of creating new clusters will gradually decrease.

The electronic conductivity data in Figure 16 provide a means of monitoring the oxidation of Fe^{2+} ions to Fe^{3+}, since the conductivity is a maximum when the amounts of these species are equal. Unfortunately, the 3-D conductivity of these materials is not high and it would be very useful to produce single crystals to allow determination of the anisotropic nature of the conductivity. It would also be interesting to synthesise and characterise materials containing some $2^{nd}/3^{rd}$ row transition metal ions into the chains of octahedra in an attempt to enhance the conductivity.

The temperature at which oxidation is rapid suggests that oxygen diffusion within the channels of oxidised schafarzikite phases is high at low temperatures, but it is not straightforward to quantify this because of the electronic component and the difficulty in achieving high quality sintered ceramic samples owing to sample instability above ~ 500ºC. Further studies in this area are ongoing and will be reported separately. Nevertheless, the

existence of molecular sized channels within the structural framework, and the incorporation of interstitial oxygen within them, suggests that materials with this general structure have potential as oxidation catalysts and electrocatalysts. In this respect, the wide range of transition metal cations that can be contained within the chains of octahedra could provide a means of broadening the range of catalytic potential. Examination of cations such as Ru^{4+} and Pt^{4+} would be of particular interest because of the possible enhancement to electronic conductivity. The materials studied here may also have high oxide ion conductivity, but their high relative molecular mass and toxicity is a limiting factor for their use in many energy applications.

5. Conclusions

This study has revealed that phases related to $FeSb_2O_4$ undergo a unique low temperature oxidation in air or oxygen: simultaneous oxidation of Fe^{2+} to Fe^{3+} and Sb^{3+} to Sb^{5+} occurs, and charge balance is achieved by oxide ions entering the structural channels and bonding to Sb in the channel walls. The resulting Sb^{5+} ions remain in the channel wall sites to provide a mixture of Sb^{3+} and Sb^{5+}. It is not simple for the interstitial oxide ion site to satisfy the bonding requirements of both Sb^{3+} and Sb^{5+} but cluster formation achieves a stable local configuration comprising one 5-coordinate Sb^{5+} ion, two interstitial O^{2-} ions and two 4-coordinate Sb^{3+} ions. Moreover, it also rationalises all other experimental observations. At present, the electronic conductivity of schafarzikite materials is not high, but the rapid oxidation/insertion reaction that occurs at ~ 350°C suggests that the interstitial O^{2-} ions may have high mobility. Improvement of the electronic component of conductivity should provide interesting possibilities for elctrocatalyst behaviour of materials with this structure, *eg* as cathodes for low temperature devices such as fuel cells and ceramic oxygen generator (COG) membranes.

6. Supporting Information

Full experimental details: synthesis, thermal characterisation, structural characterisation (XRPD, NPD; Raman, Mössbauer, and NMR spectroscopy) and conductivity measurements. XPS spectra.

7. Acknowledgements

We thank EPSRC for financial support of this research (EP/L014114/1) and EPSRC, EU and ILL for the provision of NPD facilities. We are grateful to Dr Vladimir Pomjakushin for assistance in collecting the NPD data at PSI. We also thank Prof Chris McConville and Dr Marc Walker for the provision of XPS data. The X-ray diffractometers and Raman spectrometer used in this research were obtained through Birmingham Science City: Creating and Characterising Next Generation Advanced Materials (West Midlands Centre for Advanced Materials Project 1), with support from Advantage West Midlands (AWM) and part funded by the European Regional Development Fund (ERDF). We are grateful to Johnson Matthey for allowing us to use dedicated apparatus for the exchange of ^{17}O-enriched oxygen with samples heated at 350°C. JVH thanks the EPSRC, the University of Warwick and the Birmingham Science City Program for partial funding of the solid state NMR infrastructure at Warwick. The latter program accessed the Birmingham Science City Advanced Materials Project 1: Creating and Characterising Next Generation Advanced Materials, which derived support from Advantage West Midlands (AWM) and the European Regional Development Fund (ERDF). The UK 850 MHz National High Field Solid State NMR Facility used in this research was funded by EPSRC and BBSRC, as well as the University of Warwick including via part funding through Birmingham Science City

Advanced Materials Projects 1 and 2 supported by Advantage West Midlands (AWM) and the European Regional Development Fund (ERDF).

Data associated with the results shown in this paper are accessible from the University of Birmingham Archive: http://epapers.bham.ac.uk/XXXX/.

References

(1) Gonzalo J. A.; Cox D. E.; Shirane G. Magnetic structure of $FeSb_2O_4$. *Phys. Rev.*, **1966**, *147*, 415-418.

(2) Atanasova M. T.; Strydom A. M.; Schutte C. J. H.; Prinsloo L. C.; Focke W. W. Crystal structure and magnetic properties of $CuSb_2O_4$. *J. Mater. Sci.*, **2014**, *49*, 3497-3510.

(3) Gavarri J. R.; Calvarin G.; Chardon B. MeX_2O_4 isomorphic compounds - anisotropic thermal-expansion and magnetic order in $mMnSb_2O_4$ *J. Solid State Chem.*, **1983**, *47*, 132-142.

(4) Koyama E.; Nakai I.; Nagashima K. Hydrothermal synthesis of single-crystal of $FeSb_2O_4$ and isostructural compounds. *Nippon Kagaku Kaishi*, **1979**, *6*, 793-795.

(5) Ståhl S. The crystal structure of $ZnSb_2O_4$ and isomorphous compounds. *Arkiv Kemi, Min. och Geol.*, **1943**, *17 B*, 1-7.

(6) Tammann G. Chemical reaction in powder form between two types of crystal. *Z. Anorg. Allg. Chem.*, **1925**, *149*, 21-34.

(7) Witteveen H. T. Magnetic susceptibility of $NiAs_2O_4$ and $NiSb_2O_4$. *Solid State Commun.*, **1971**, *9*, 1313-1315.

(8) Dordevic T.; Wittwer A.; Jaglicic Z.; Djerdj I. Hydrothermal synthesis of single crystal $CoAs_2O_4$ and $NiAs_2O_4$ compounds and their magnetic properties. *RSC Adv.*, **2015**, *5*, 18280-18287.

(9) Kumada N.; Yonesaki Y.; Takei T.; Kinomura N.; Wada S. Preparation and crystal structure of a new tin titanate containing Sn^{2+}; Sn_2TiO_4. *Mater. Res. Bull.*, **2009**, *44*, 1298-1300.

(10) Ohara S.; Takizawa H.; Hayashi Y. Solid-state Synthesis of Sn_2TiO_4: A New Synthetic Strategy for Direct Synthesis of Sn^{2+} Compounds Using Microwave Irradiation. *Chem. Lett.*, **2010**, *39*, 364-365.

(11) Abakumov A. M.; Rozova M. G.; Antipov E. V.; Hadermann J.; Van Tendeloo G.; Lobanov M. V.; Greenblatt M.; Croft M.; Tsiper E. V.; Llobet A.; Lokshin K. A.; Zhao Y. S. Synthesis, cation ordering, and magnetic properties of the $(Sb_{1-x}Pb_x)_2(Mn_{1-y}Sb_y)O_4$ solid solutions with the Sb_2MnO_4-type structure. *Chem. Mater.*, **2005**, *17*, 1123-1134.

(12) de Laune B. P.; Greaves C. Structural and magnetic characterisation of $CoSb_2O_4$, and the substitution of Pb^{2+} for Sb^{3+} *J. Solid State Chem.*, **2012**, *187*, 225-230.

(13) Whitaker M. J.; Bayliss R. D.; Berry F. J.; Greaves C. The synthesis, structure, magnetic and electrical properties of $FeSb_{2-x}Pb_xO_4$. *J. Mater. Chem.*, **2011**, *21*, 14523-14529.

(14) Cumby J.; de Laune B. P.; Greaves C. The Structures and Magnetic Properties of $Fe_xCo_{1-x}Sb_2O_4$ and $Mn_xCo_{1-x}Sb_2O_4$, $0 \leq x \leq 1$. *J. Mater. Chem. C*, **2016**, *4*, 201-208.

(15) Fjellvåg H.; Kjekshus A. Crystal and magnetic structure of $MnSb_2O_4$. *Acta Chem. Scand. A*, **1985**, *39*, 389-395.

(16) Caslin K.; Kremer R. K.; Razavi F. S.; Schulz A.; Munoz A.; Pertlik F.; Liu J.; Whangbo M. H.; Law J. M. Characterization of the spin-1/2 linear-chain ferromagnet $CuAs_2O_4$. *Phys. Rev. B*, **2014**, *89*, 014412.

(17) Minh N. Q. Ceramic Fuel Cells. *J. Am. Ceram. Soc.*, **1993**, *76*, 563-588.

(18) (a) Chroneos A.; Yildiz B.; Tarancon A.; Parfitt D.; Kilner J. A. Oxygen diffusion in solid oxide fuel cell cathode and electrolyte materials: mechanistic insights from atomistic simulations. *Energy Environ. Sci.*, **2011**, *4*, 2774-2789; (b) Kushima A.; Parfitt D.; Chroneos A.; Yildiz B.; Kilner J. A.; Grimes R. W. Interstitialcy diffusion of oxygen in tetragonal $La_2CoO_{4+\delta}$. *Phys. Chem. Chem. Phys.*, **2011**, *13*, 2242-2249.

(19) Brown I. D.; Altermatt D. Bond-Valence Parameters Obtained from a Systematic Analysis of the Inorganic Crystal Structure Database. *Acta Crystallogr.*, **1985**, *B41*, 244-247.

(20) Tallman R. L.; Margrave J. L.; Bailey S. W. The crystal structure of sodium peroxide. *J. Am. Chem. Soc.*, **1957**, *79*, 2979-2980.

(21) Eysel H. H.; Thym S. Raman-spectra of peroxides. *Z. Anorg. Allg. Chem.*, **1975**, *411*, 97-102.

(22) Kharbish S. Raman spectra of minerals containing interconnected As(Sb)O_3 pyramids: trippkeite and schafarzikite. *J. Geosci.*, **2012**, *57*, 53-62.

(23) (a) Donaldson J. D.; Kjekshus A.; Nicholson D. G.; Rakke T. Properties of Sb-compounds with rutile-like structures. *Acta. Chem. Scand. A*, **1975**, *29*, 803-809; (b) Reimers J. N.; Greedan J. E.; Stager C. V.; Kremer R. Crystal-structure and magnetism in $CoSb_2O_6$ and $CoTa_2O_6$. *J. Solid State Chem.*, **1989**, *83*, 20-30.

(24) de Laune B. P.; Berry F. J.; Marco J. F.; Horswell S. L.; Greaves C. The Structure, Chemistry and Magnetic Properties of $FePbBiO_4$. *J. Mater. Chem. C*, **2016**, *4*, 5320-5325.

(25) Ivanov S. A.; Zavodnik V. E. Crystal-structure of lead antimonate $Pb_2Sb_2O_7$. *Kristallografiya*, **1990**, *35*, 842-846.

(26) Srivastava A.; Chauhan M.; Padegaonker R. Theoretical investigation of high-pressure phase transitions in $Mg_{1-x}Sr_xO$. *Phase Transitions*, **2014,** *87*, 126-135.

(27) Svensson C. Refinement of crystal-structure of cubic antimony trioxide, Sb_2O_3. *Acta Crystallographica B*, **1975,** *31*, 2016-2018.

(28) Giroux-Maraine C; Perez G. Crystal-structure of magnesium antimonite, $MgSb_2O_4$. *Rev. Chim. Miner.*, **1975,** *12*, 427-432.

(29) Dupree R.; Smith M. E. Solid-state magnesium-25 nmr-spectroscopy. *Chem. Comm.*, **1988,** 1483-1485.

(30) (a) McCarty R. J.; Stebbins J. F. Transition Metal Dopant Cation Distributions in MgO and CaO: New Inferences from Paramagnetically Shifted Resonances in O-17, Mg-25, and Ca-43 NMR Spectra. *J. Phys. Chem. C*, **2016,** *120*, 11111-11120; (b) Kong X.; Terskikh V. V.; Khade R. L.; Yang L.; Rorick A.; Zhang Y.; He P.; Huang Y.; Wu G. Solid-State O-17 NMR Spectroscopy of Paramagnetic Coordination Compounds. *Angew. Chem. Int. Edit.*, **2015,** *54*, 4753-4757.

(31) King G.; Thomas K. J.; Llobet A. Drastic Differences between the Local and the Average Structures of $Sr_2MSbO_{5.5}$ (M = Ca, Sr, Ba) Oxygen-Deficient Double Perovskites. *Inorg. Chem.*, **2012**, *51*, 13060-13068.

Tables

Table 1. Important phase compositions and their Fe^{2+} content.

Composition	Amount of Fe^{2+} per formula unit
$Co_{0.75}Fe_{0.25}Sb_2O_4$	0.25
$Mg_{0.75}Fe_{0.25}Sb_2O_4$	0.25
$FeSb_{1.25}Pb_{0.75}O_4$	$0.25Fe^{2+}$ ($+0.75Fe^{3+}$)
$Co_{0.25}Fe_{0.75}Sb_{1.75}Pb_{0.25}O_4$	$0.50Fe^{2+}$ ($+0.25Fe^{3+}$)

Table 2. Structural parameters for $FeSb_{1.25}Pb_{0.75}O_{4+y}$ from NPD data.

Atom	Position	*X*	*y*	*z*	$100\times U_{iso}$ ($Å^2$)	Occupancy
Fe	4*d*	0.0	0.0	0.25	2.19(6)	1.0
Sb/Pb	8*h*	0.1542(3)	0.1557(3)	0.0	2.82(6)	0.625/0.375
O1	8*g*	0.6701(2)	0.1701(2)	0.25	3.90[#]	1.0
O2	8*h*	0.0981(3)	0.6278(3)	0.0	2.64(8)	1.0
O3	16*i*	0.540(5)	0.417(3)	0.254(7)	3(1)	0.059(4)
[#]Anisotropic parameters (all $\times 100/Å^2$): U_{11} 4.5(1), U_{22} 4.5(1), U_{33} 2.7(2); U_{12} -2.4(1); U_{13} -0.8(1) U_{23} 0.8(1)						
$P4_2/mbc$; a = 8.4063(3) Å, b = 8.4063(3) Å, c = 6.0443(3) Å χ^2 = 2.24; R_{wp} = 0.051						

Table 3. Selected bond distances and bond valence sums (using the r_o parameter for Fe^{3+})[26] for $FeSb_{1.25}Pb_{0.75}O_{4+y}$.

Bond distances / Å		BVS
Fe – O1	2.023(3) [×2]	
– O2	2.029(2) [×4]	2.91
Sb/Pb – O1	2.108(2)	
Sb/Pb – O2	2.095(4) [×2]	
Sb/Pb – O3	1.91(4), 2.30(5)	
O3 – O3	1.09(3), 1.54(5)	

Table 4. ^{57}Fe and ^{121}Sb Mössbauer parameters for $Co_{0.25}Fe_{0.75}Sb_{1.75}Pb_{0.25}O_4$ and $Co_{0.25}Fe_{0.75}Sb_{1.75}Pb_{0.25}O_{4+y}$ after heating at 350°C and 500°C.

Sample	Temperature of measurement / K	Δ or e^2qQ_g (± 0.06) / mm s^{-1}	δ (± 0.03) / mm s^{-1}	Area (± 5) / %
$Co_{0.25}Fe_{0.75}Sb_{1.75}Pb_{0.25}O_4$				
Fe^{2+}	298	1.84	1.06	58
Fe^{3+}	298	0.84	0.41	42
Sb^{3+}	298	+8.35	-11.02	100
Sb^{5+}	298	-	-	0
Sb^{3+}	90	+18.63	-11.08	100
Sb^{5+}	90	-	-	0
$Co_{0.25}Fe_{0.75}Sb_{1.75}Pb_{0.25}O_{4+y}$ heated at 350°C				
Fe^{2+}	298	-	-	0
Fe^{3+}	298	0.67	0.39	100
Sb^{3+}	298	+8.44	-11.80	78
Sb^{5+}	298		-0.50	22
Sb^{3+}	90	+17.57	-12.14	82
Sb^{5+}	90		-0.55	18
$Co_{0.25}Fe_{0.75}Sb_{1.75}Pb_{0.25}O_{4+y}$ heated at 500°C				
Fe^{2+}	298	-	-	0
Fe^{3+}	298	0.84	0.37	100
Sb^{3+}	298	+8.16	-12.50	53
Sb^{5+}	298		-0.57	47
Sb^{3+}	90	+15.88	-12.59	58
Sb^{5+}	90		-0.46	42

Table 5. The experimentally determined and GIPAW DFT calculated NMR parameters (δ_{iso}, C_Q, η and P_Q) from the diamagnetic MgO, $Sb_2{}^{17}O_3$ and $MgSb_2{}^{17}O_4$ systems.

			Experimental							CASTEP				
Sample	Site	Isotope	δ_{iso} (ppm)	δ_{iso} Error (ppm)	C_Q (MHz)	η	P_Q (MHz)	P_Q Error (MHz)	Geom. Opt.	σ (ppm)	δ_{iso} (ppm)	C_Q (MHz)	η	P_Q (MHz)
MgO[26]	1	^{25}Mg	26						No	535.2	26[a]	0	0	0
Sb_2O_3[27]	1	^{17}O	167		5.2	0.99			No	70.8	167[b]	5.93	0.93	6.73
$MgSb_2O_4$[28]	1	^{17}O	−11	±3			4.9	±0.3	No	50.2	146.1	4.47	0.00	4.47
	2	^{17}O	139	±4			3.5	±0.6		67.1	163.0	5.49	0.56	5.77
	1	^{25}Mg	19		6.4	0.00				528.9	19.8	5.89	0.14	5.90
$MgSb_2O_4$[28]	1	^{17}O	−11	±3			4.9	±0.3	Yes	33.3	104.1	4.64	0.00	4.64
	2	^{17}O	139	±4			3.5	±0.6		55.7	151.6	5.62	0.54	5.89
	1	^{25}Mg	19		6.4	0.00				531.5	22.3	5.56	0.04	5.56

[a] σ_{ref} from Dupree and Smith.[29]

[b] measured σ_{ref} given in Figure 14(e).

Figure Captions

Figure 1.
The schafarzikite structure viewed (a) approximately along [001] showing the empty channels and (b) along [110]. Elements are represented as colored spheres: Fe^{2+} (A site; blue), Sb^{3+} (B site; black), and O^{2-} in the O2, equatorial, (red) and O1, apical, (yellow) positions. FeO_6 octahedra are grey.

Figure 2.
TGA plots for $CoSb_2O_4$ (green), $Mg_{0.25}Fe_{0.75}Sb_2O_4$ (brown), $Co_{0.25}Fe_{0.75}Sb_{1.75}Pb_{0.25}O_4$ (purple) heated in an O_2 atmosphere at 10°C min^{-1} to 800°C.

Figure 3.
The increase in oxygen content per formula unit (pfu) as a function of initial Fe^{2+} content pfu from TGA data for the three series indicated. The results are compared to those expected assuming only oxidation of Fe^{2+} to Fe^{3+}.

Figure 4.
Difference Fourier map for $FeSb_{1.25}Pb_{0.75}O_{4.24}$ showing additional neutron scattering near the centre of the channel running along [001] and located at (0,0,*z*), see Fig.1. The position corresponding to the O3 site of Table 2 is marked.

Figure 5.
The Rietveld refinement profiles for $FeSb_{1.25}Pb_{0.75}O_{4.24}$ showing raw data (red crosses), fitted profile (green) and difference profile (mauve). Reflection positions are marked as vertical bars.

Figure 6.
The refined structure of $FeSb_{1.25}Pb_{0.75}O_{4.24}$ highlighting the interstitial oxygen positions. All O are red, Sb/Pb black and Fe blue. A possible O–O linkage (O–O 1.54(5) Å) is shown.

Figure 7.
In situ NPD data for the oxidation of $Co_{0.25}Fe_{0.75}Sb_{1.75}Pb_{0.25}O_4$. (a) The raw data at 320°C (red) and background (black) from an empty quartz tube at 300°C. (b) The corrected raw data after background subtraction. (c) Rietveld refinement profiles showing raw data (red crosses), fitted profile (green) and difference profile (mauve); reflection positions are marked as vertical bars.

Figure 8.
The variation with temperature of various structural parameters for $Co_{0.25}Fe_{0.75}Sb_{1.75}Pb_{0.25}O_4$ on heating in oxygen: (a) O3 site occupancy; (b) unit cell parameters; (c) unit cell volume; (d) average bond distance within the MO_6 octahedra showing values predicted for oxidation of Fe^{2+} to Fe^{3+}; (e) cation separation across the channel (Sb/Pb – Sb/Pb); (f) average Sb/Pb – O (excluding interstitial O3). Error bars are included (±1esd) for all plots.

Figure 9.
Raman spectra of $Co_{0.75}Fe_{0.25}Sb_2O_4$ and the oxidised product, $Co_{0.75}Fe_{0.25}Sb_2O_{4+y}$.

Figure 10.
Total correlation function *G(r)* against pair distance (*r*) for $Co_{0.25}Fe_{0.75}Sb_{1.75}Pb_{0.25}O_4$ (black) and $Co_{0.25}Fe_{0.75}Sb_{1.75}Pb_{0.25}O_{4+y}$ (red).

Figure 11.
Mössbauer spectra for $Co_{0.25}Fe_{0.75}Sb_{1.75}Pb_{0.25}O_4$: (a) ^{57}Fe spectrum showing the individual fitting of Fe^{2+} (green line) and Fe^{3+} (blue line), and the overall fit (red line); (b) ^{121}Sb spectrum showing the fit to Sb^{3+} alone (blue line).

Figure 12.
Mössbauer spectra for $Co_{0.25}Fe_{0.75}Sb_{1.75}Pb_{0.25}O_4$ after heating at 350°C: (a) ^{57}Fe spectrum showing the fitting to Fe^{3+} (blue line); (b) ^{121}Sb spectrum showing the individual fits for Sb^{3+} (blue line) and Sb^{5+} (green line), and the overall fit (red line).

Figure 13.
Mössbauer spectra for $Co_{0.25}Fe_{0.75}Sb_{1.75}Pb_{0.25}O_4$ after heating at 500°C: (a) ^{57}Fe spectrum showing the fitting to Fe^{3+} (blue line); (b) ^{121}Sb spectrum showing the individual fits for Sb^{3+} (blue line) and Sb^{5+} (green line), and the overall fit (red line).

Figure 14.
The (a) multi-B_0 field ^{17}O MAS NMR data (ν_r = 20 kHz), (b) ^{17}O 3QMAS (ν_r = 20 kHz) and (c) graphical analysis of the multi-B_0 field yielding estimates of δ_{iso} and the quadrupole product P_Q from hydrothermally ^{17}O labelled $MgSb_2O_4$. The ^{25}Mg MAS NMR data from ^{25}Mg enriched high temperature calcined $MgSb_2O_4$ is shown in (d), while the ^{17}O MAS NMR data from hydrothermally ^{17}O labelled Sb_2O_3 is shown in (e).

Figure 15.
The ^{17}O MAS NMR data (ν_r = 20 kHz) from (a) diamagnetic $MgSb_2O_4$, (b) $Co_{0.50}Fe_{0.50}Sb_2O_{4+y}$, (c) $Co_{0.25}Fe_{0.75}Sb_{1.75}Pb_{0.25}O_{4+y}$, (d) $Mg_{0.25}Fe_{0.75}Sb_{1.75}Pb_{0.25}O_{4+y}$ and (e) $Mg_{0.50}Fe_{0.50}Sb_2O_{4+y}$. The ^{17}O signal from the ZrO_2 rotor is indicated as 'R' and the signal from the channel ^{17}O is represented schematically by a dashed arc.

Figure 16.
Electronic conductivity data for a pellet with initial composition $Co_{0.50}Fe_{0.50}Sb_2O_4$. (a) Variation of conductivity with temperature for heating and cooling in air; the blue data points are from a similar pellet heated in dry nitrogen. (b) Log(conductivity) against 1000/T for the data shown in (a); the red lines are linear fits to the sections of data indicated. (c) Variation of conductivity with time at 350°C after switching the gas from dry nitrogen to dry oxygen.

Figure 17.
The proposed defect cluster comprising two 4-coordinate Sb^{3+} ions (black), two interstitial O^{2-} ions (orange) and one 5-coordinate Sb^{5+} ion (black) viewed (a) approximately along [010] and (b) approximately along [001]. Framework oxygen ions are shown in red and the Sb – O3 distances are marked in (a).

Figures

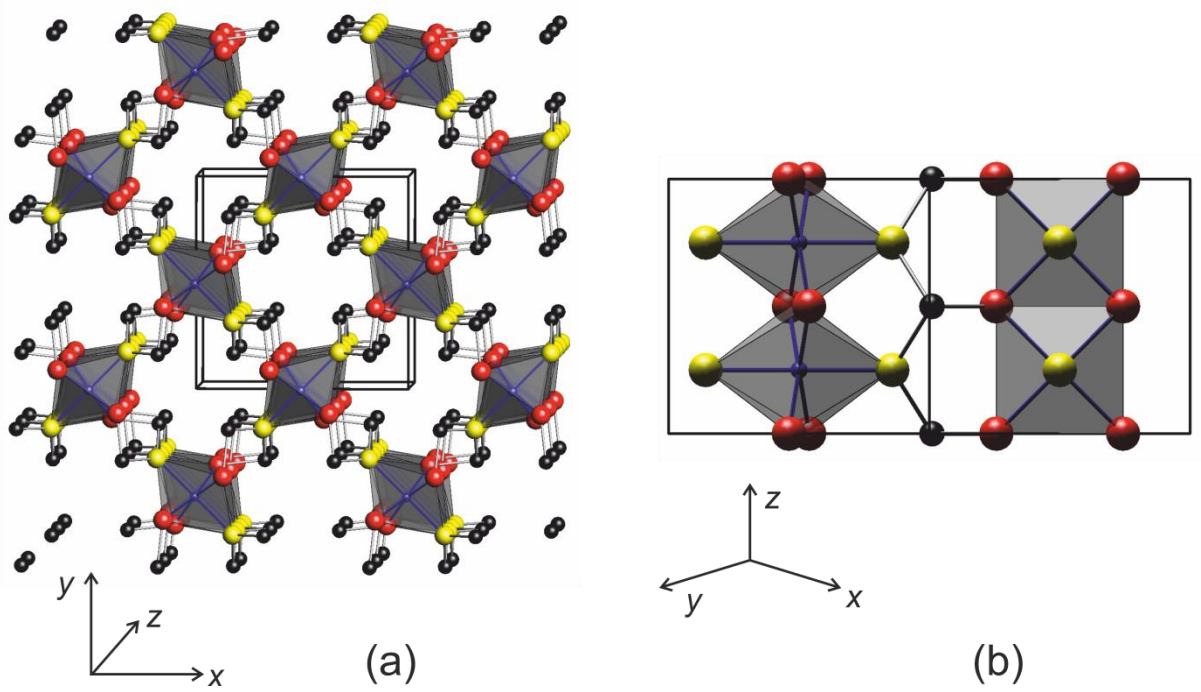

Fig.1

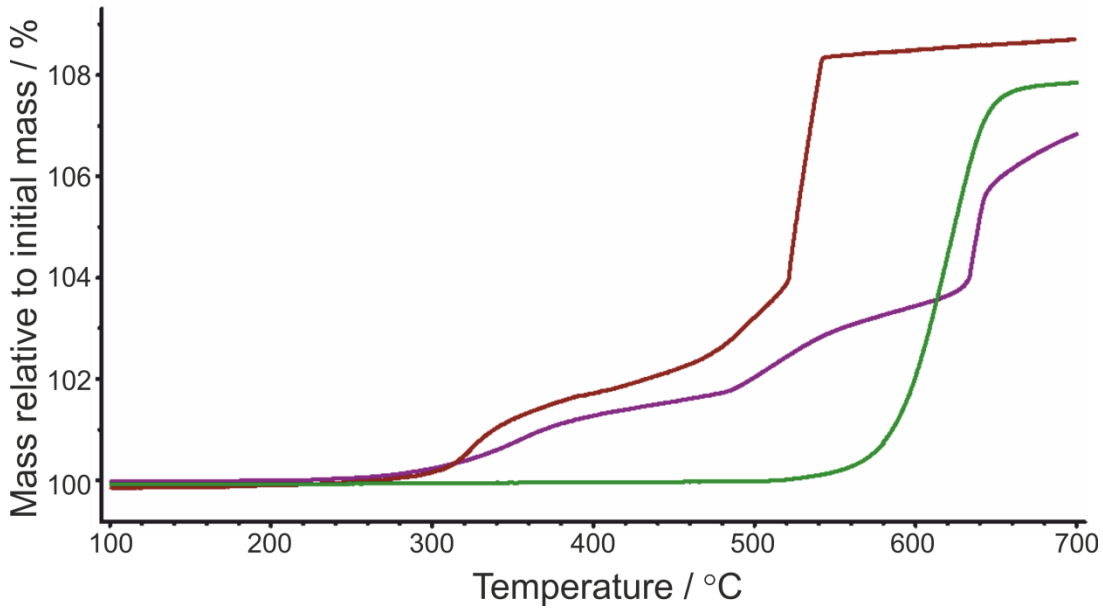

Fig.2

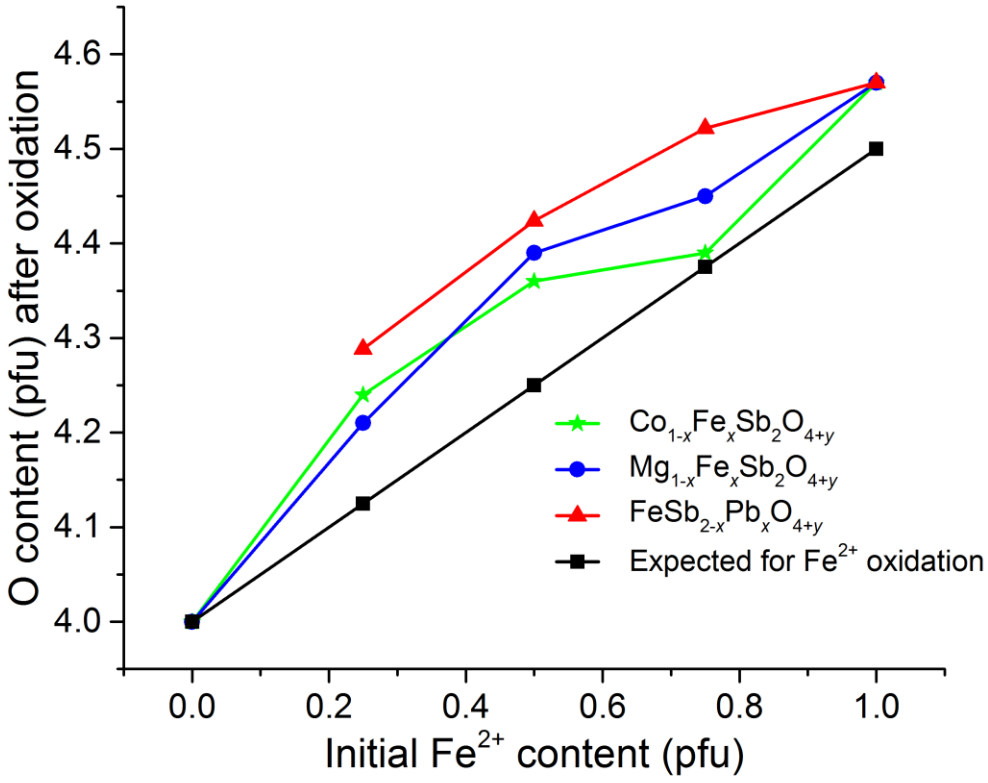
O content (pfu) after oxidation
4.6
4.5
4.4
4.3
4.2
4.1
4.0
0.0
0.2
0.4
0.6
0.8
1.0
Initial Fe2+ content (pfu)
Co1-xFexSb2O4+y
Mg1-xFexSb2O4+y
FeSb2-xPbxO4+y
Expected for Fe2+ oxidation

Fig.3

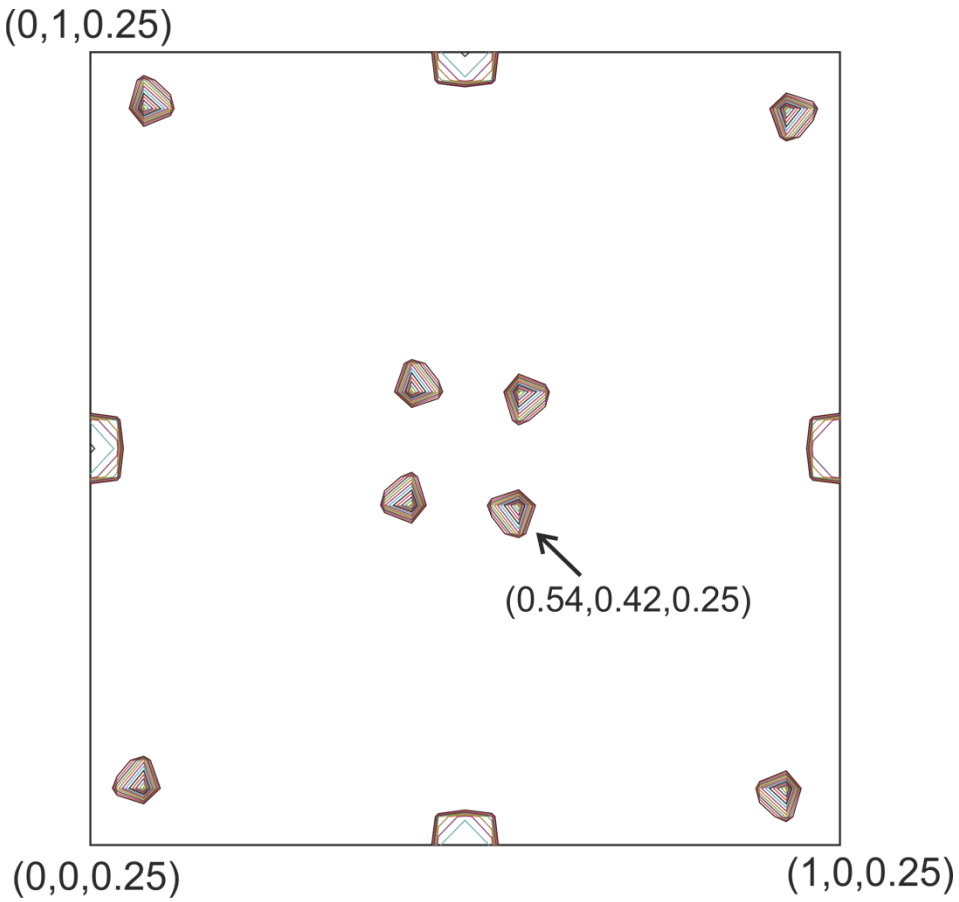

Fig.4

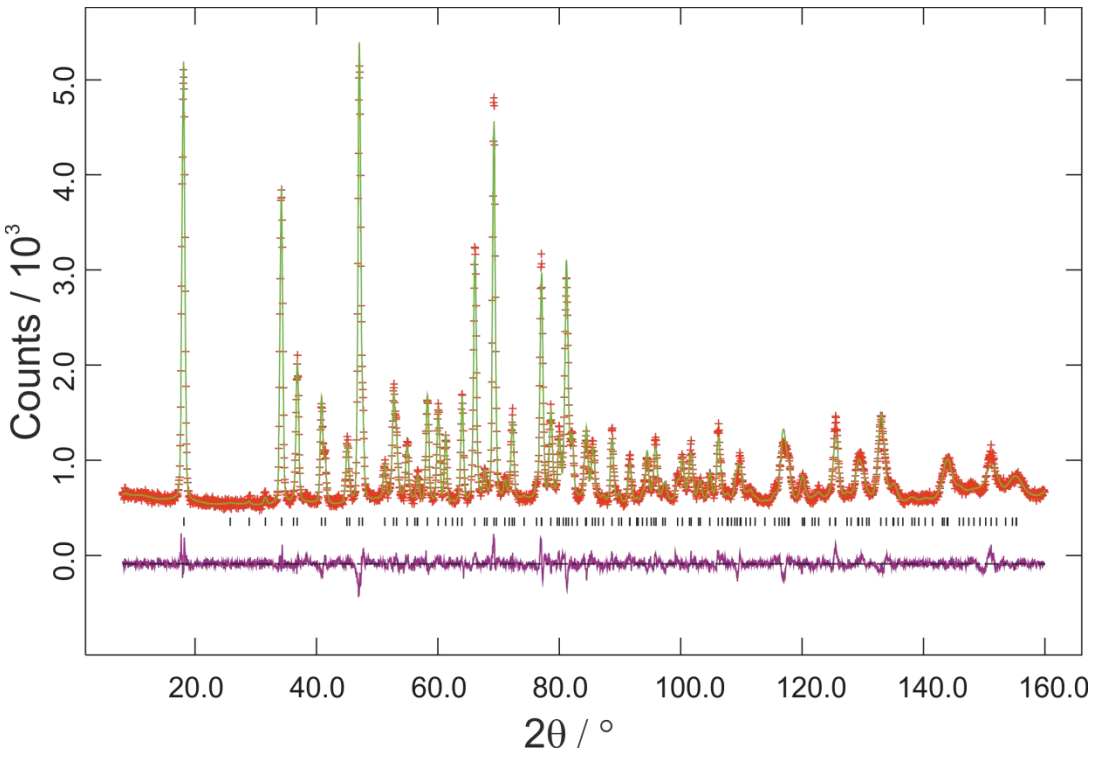
Counts / 10^3
0.0
1.0
2.0
3.0
4.0
5.0
20.0
40.0
60.0
80.0
100.0
120.0
140.0
160.0
2θ / °

Fig.5

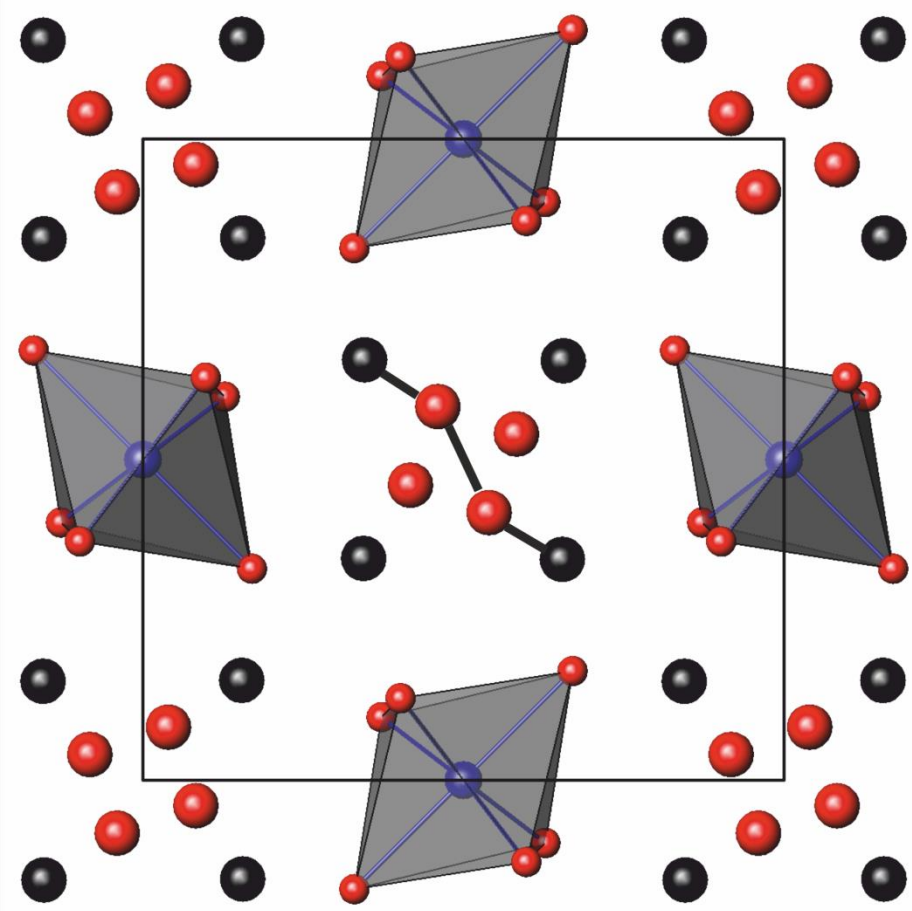

Fig.6

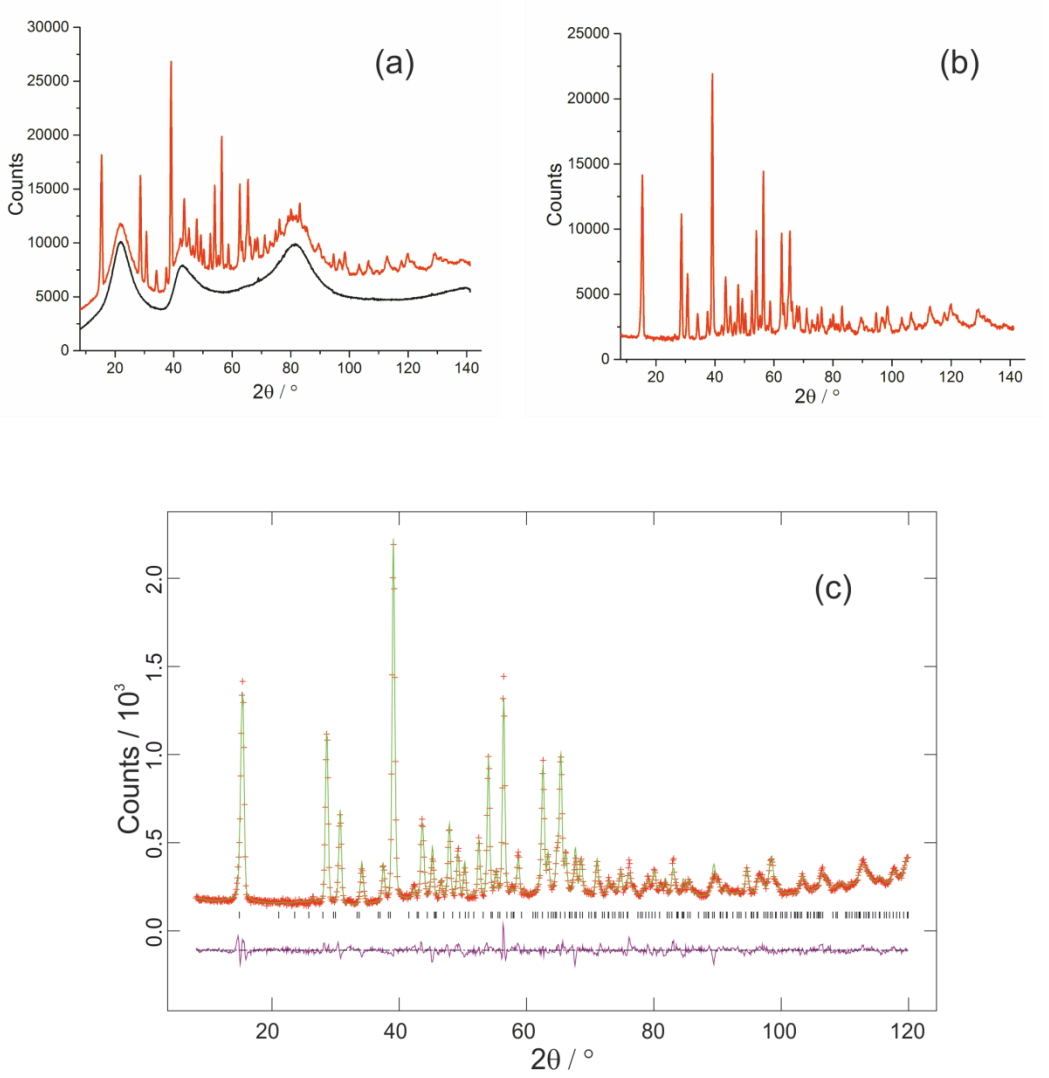

Fig.7

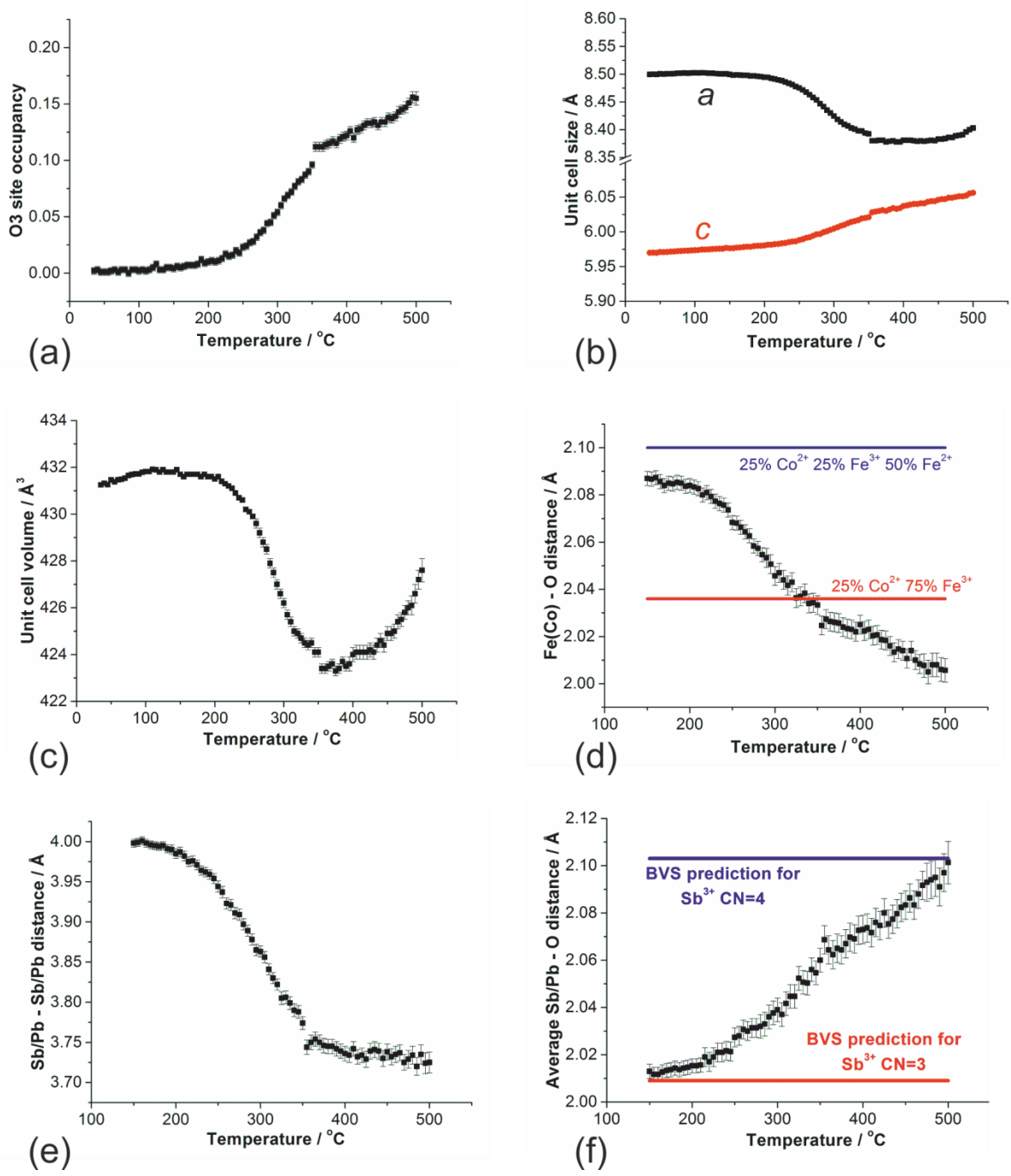
O3 site occupancy
Temperature / °C
(a)
Unit cell size / Å
a
c
Temperature / °C
(b)
Unit cell volume / Å3
Temperature / °C
(c)
Fe(Co) - O distance / Å
25% Co2+ 25% Fe3+ 50% Fe2+
25% Co2+ 75% Fe3+
Temperature / °C
(d)
Sb/Pb - Sb/Pb distance / Å
Temperature / °C
(e)
Average Sb/Pb - O distance / Å
BVS prediction for
Sb3+ CN=4
BVS prediction for
Sb3+ CN=3
Temperature / °C
(f)

Fig.8

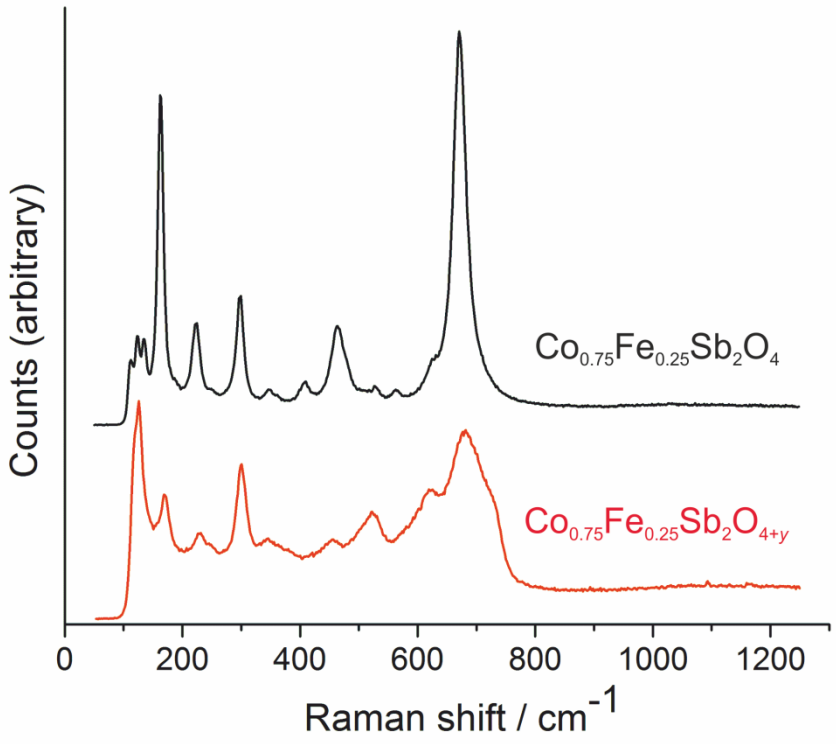
Counts (arbitrary)
Co0.75Fe0.25Sb2O4
Co0.75Fe0.25Sb2O4+y
0
200
400
600
800
1000
1200
Raman shift / cm-1

Fig.9

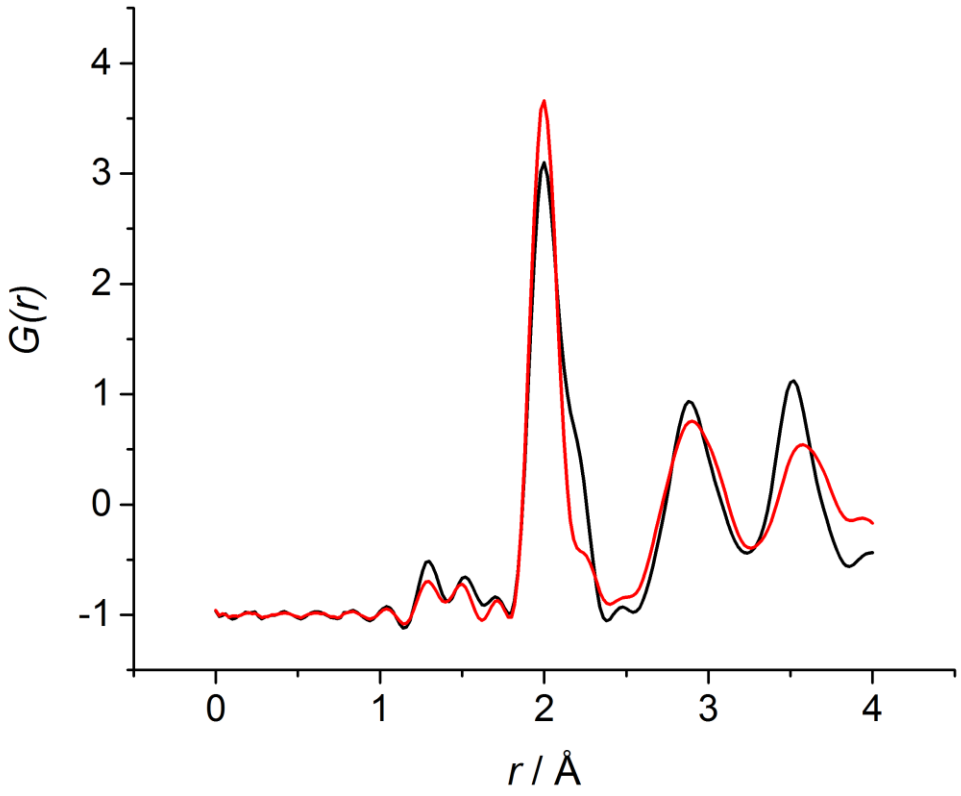

Fig.10

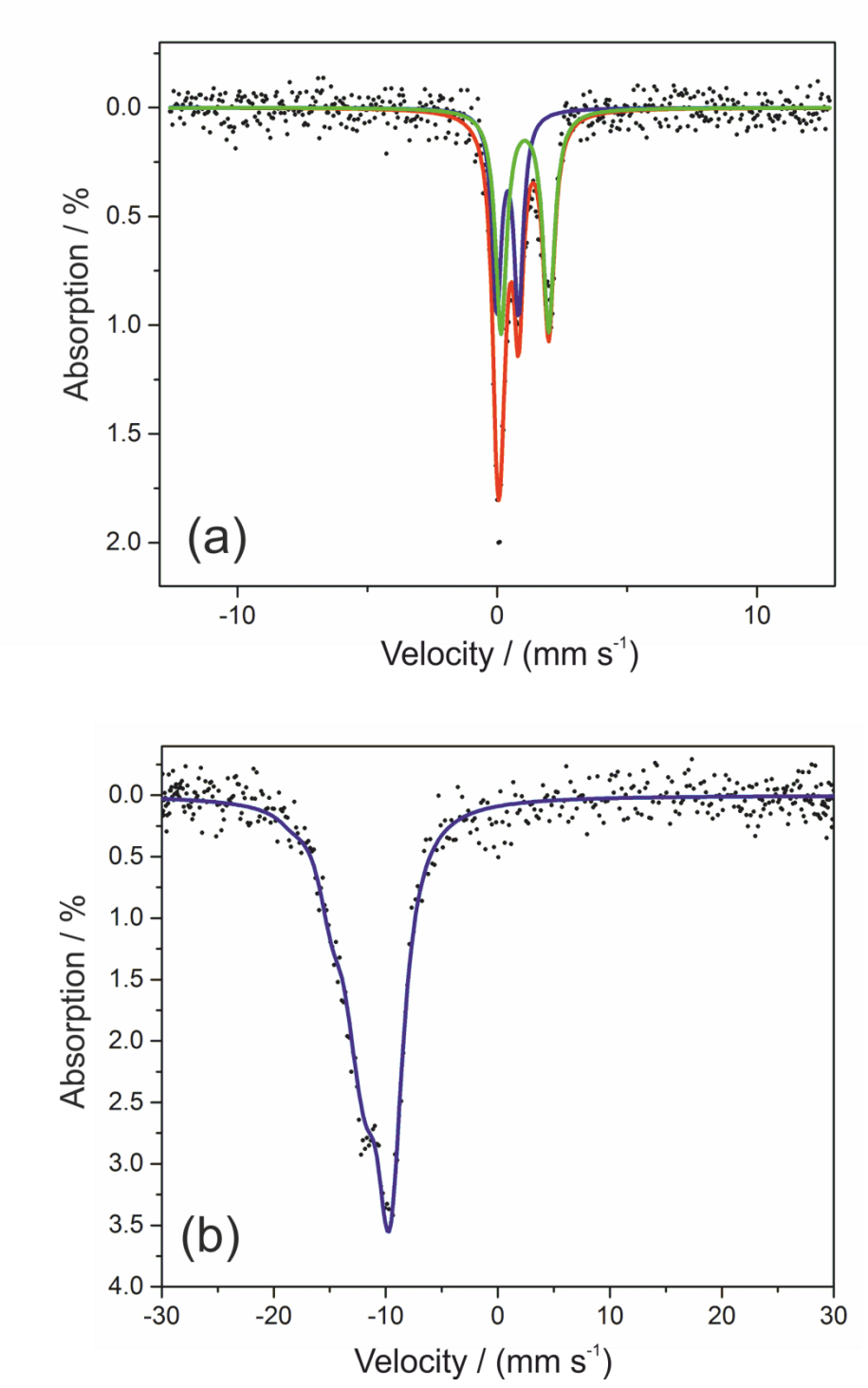
Absorption / %
0.0
0.5
1.0
1.5
2.0
(a)
-10
0
10
Velocity / (mm s-1)
Absorption / %
0.0
0.5
1.0
1.5
2.0
2.5
3.0
3.5
4.0
(b)
-30
-20
-10
0
10
20
30
Velocity / (mm s-1)

Fig.11

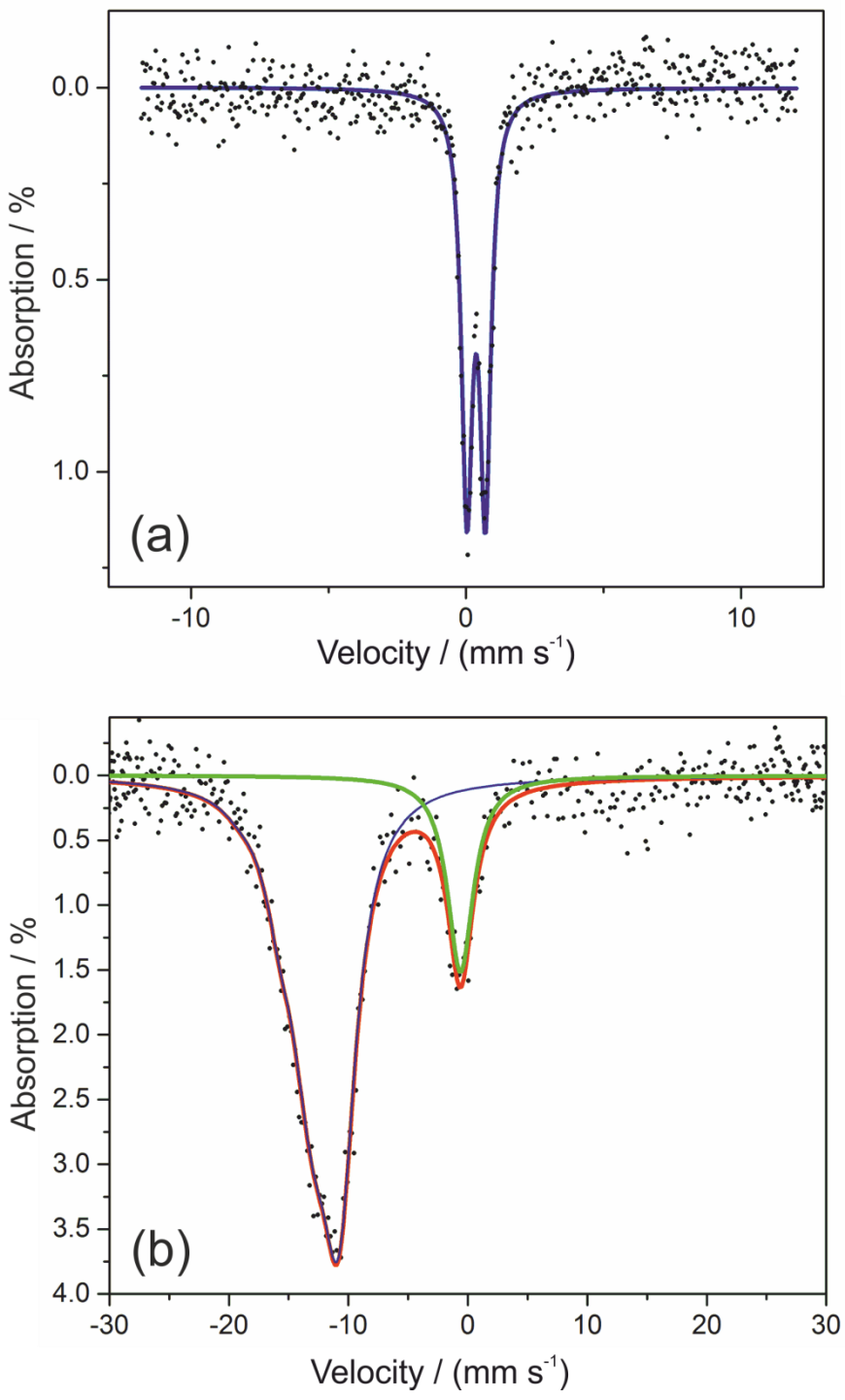
0.0
0.5
1.0
Absorption / %
(a)
-10
0
10
Velocity / (mm s-1)
0.0
0.5
1.0
1.5
2.0
2.5
3.0
3.5
4.0
Absorption / %
(b)
-30
-20
-10
0
10
20
30
Velocity / (mm s-1)

Fig.12

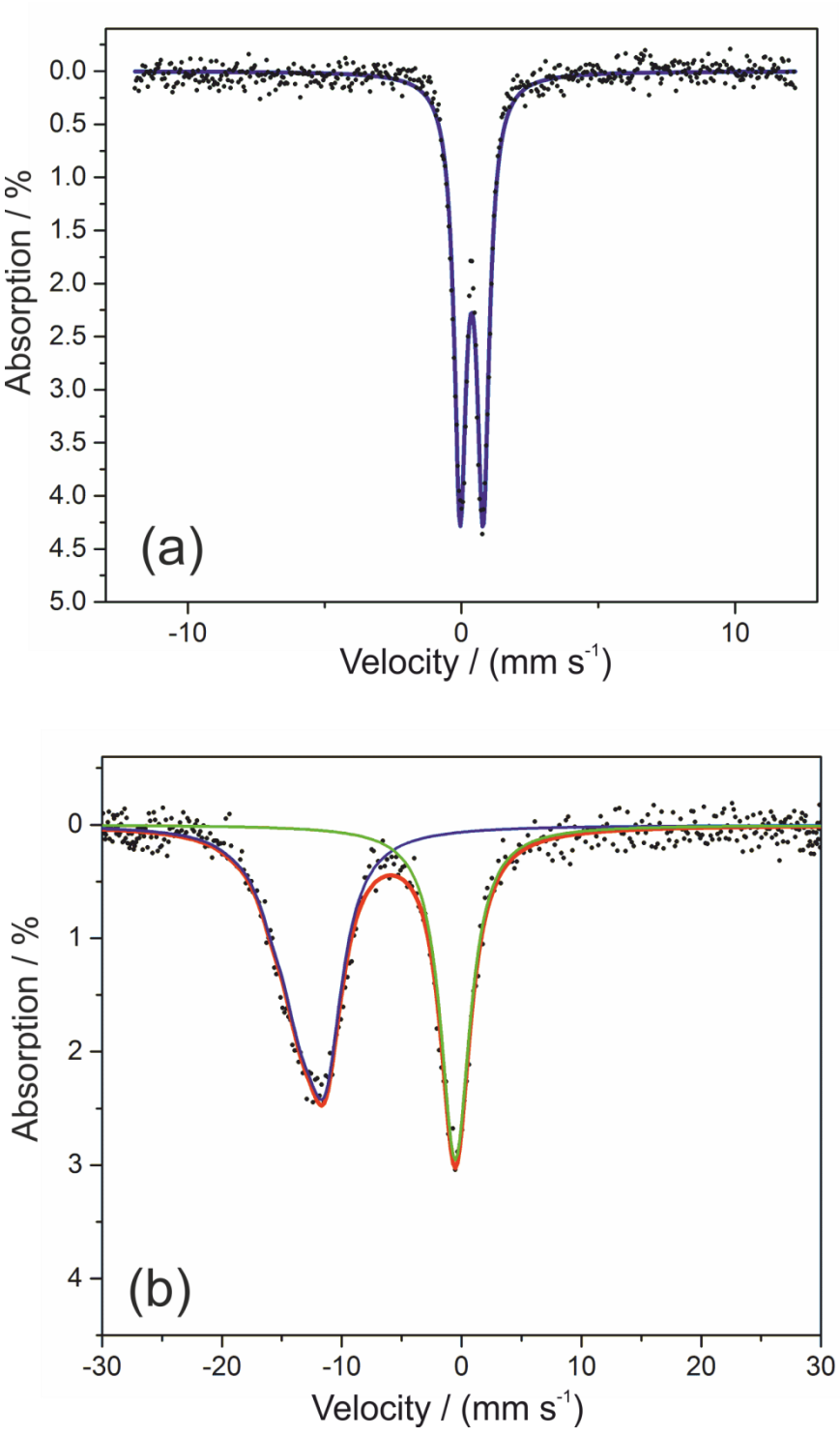
Absorption / %
0.0
0.5
1.0
1.5
2.0
2.5
3.0
3.5
4.0
4.5
5.0
(a)
-10
0
10
Velocity / (mm s-1)
Absorption / %
0
1
2
3
4
(b)
-30
-20
-10
0
10
20
30
Velocity / (mm s-1)

Fig.13

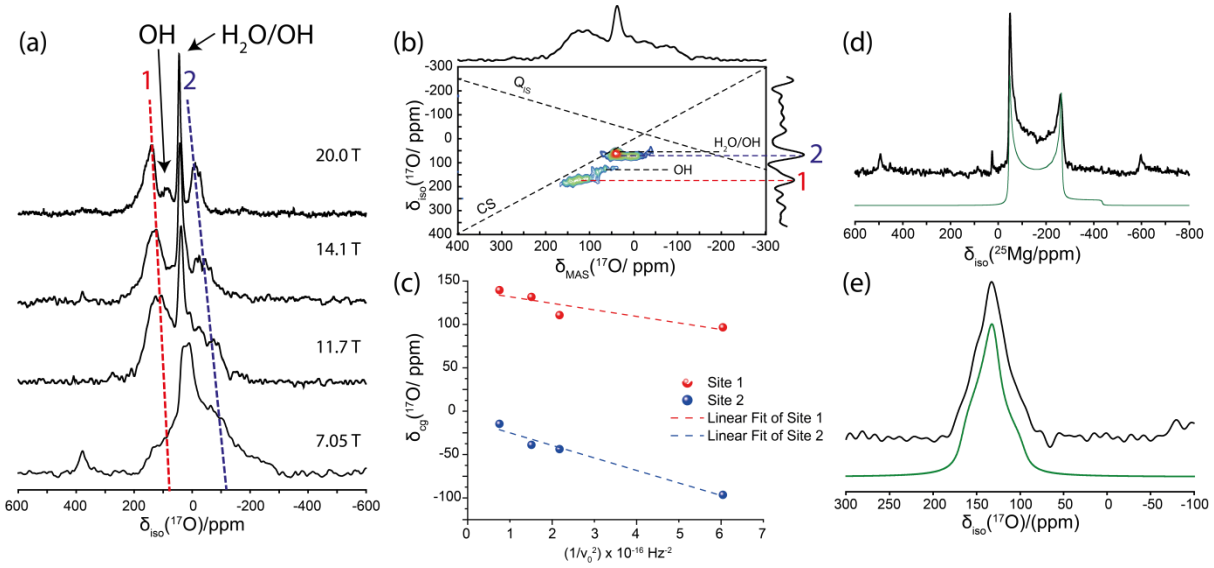
(a)
OH
H2O/OH
1
2
20.0 T
14.1 T
11.7 T
7.05 T
δiso(17O)/ppm
(b)
QIS
CS
H2O/OH
OH
δiso(17O/ ppm)
δMAS(17O/ ppm)
(c)
δcg(17O/ ppm)
Site 1
Site 2
Linear Fit of Site 1
Linear Fit of Site 2
(1/ν0²) x 10⁻¹⁶ Hz⁻²
(d)
δiso(25Mg/ppm)
(e)
δiso(17O)/(ppm)

Fig.14

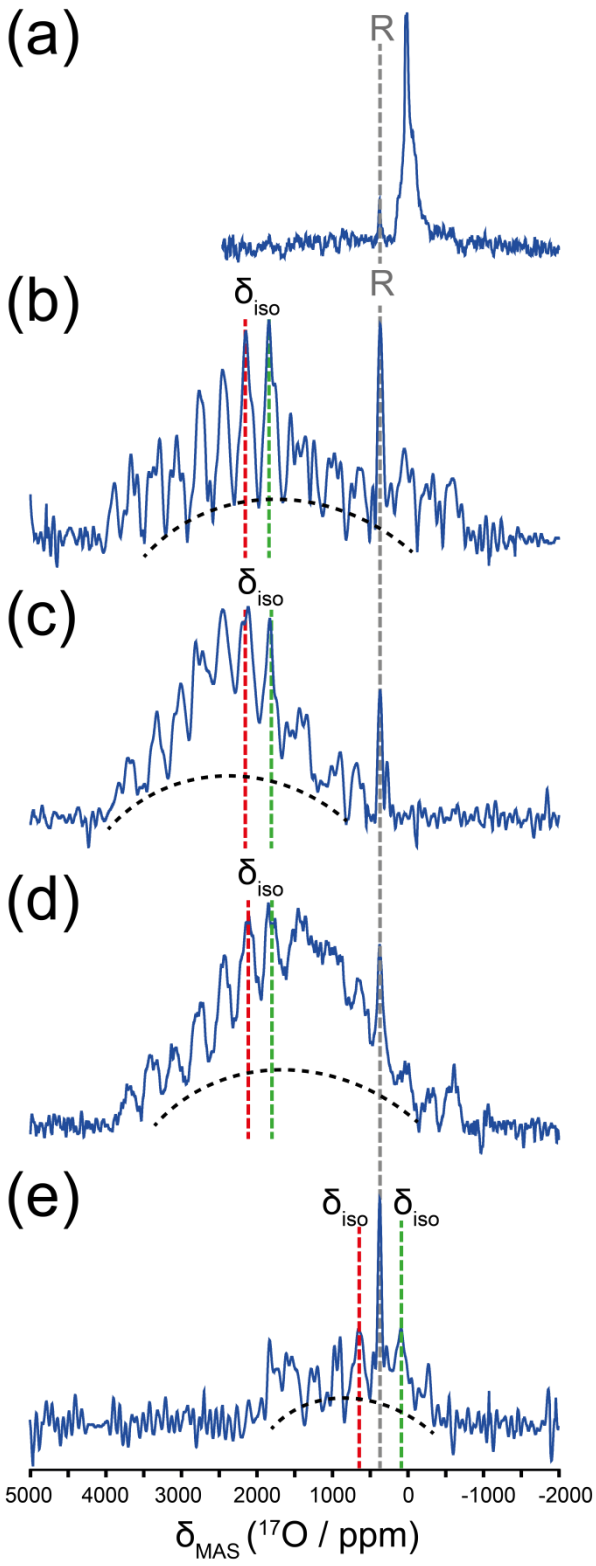
(a)
R
(b)
δiso
R
(c)
δiso
(d)
δiso
(e)
δiso
δiso
5000
4000
3000
2000
1000
0
-1000
-2000
δMAS (17O / ppm)

Fig.15

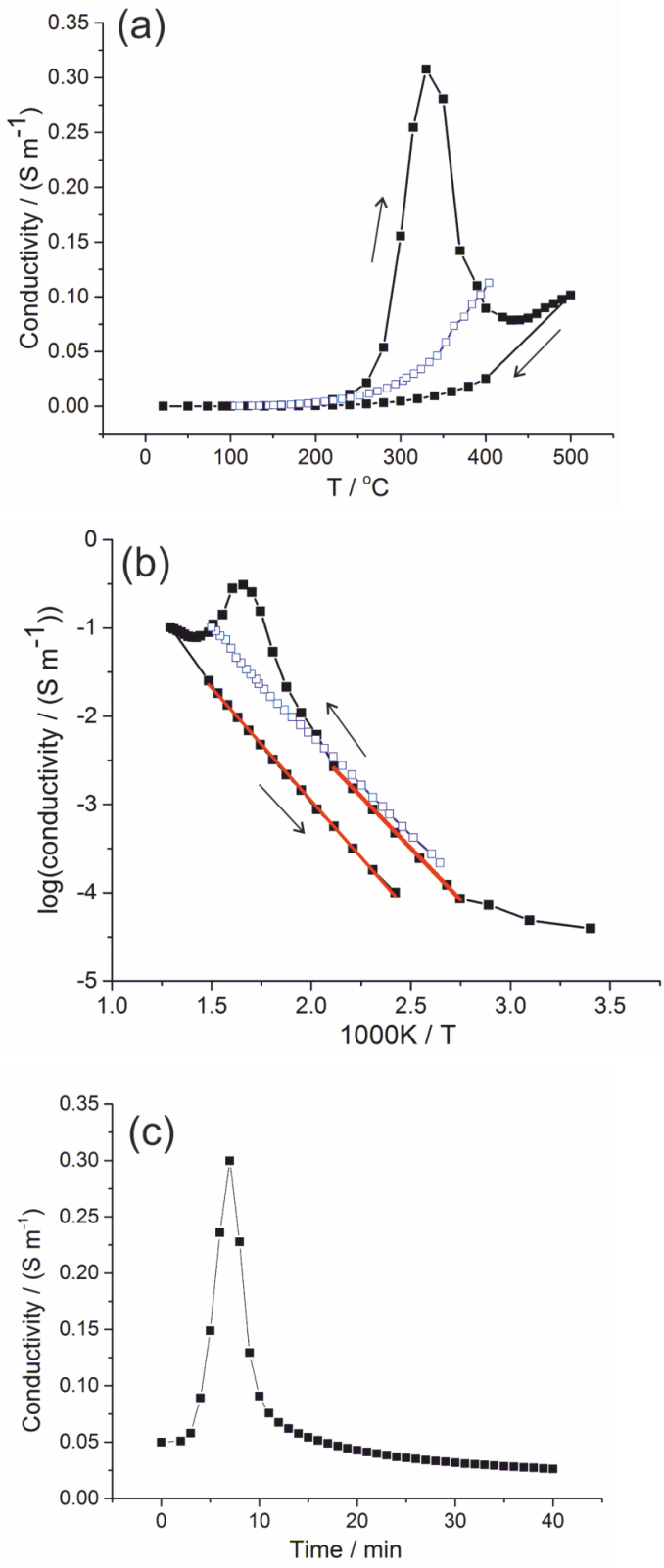
(a)
Conductivity / (S m-1)
T / °C
(b)
log(conductivity / (S m-1))
1000K / T
(c)
Conductivity / (S m-1)
Time / min

Fig.16

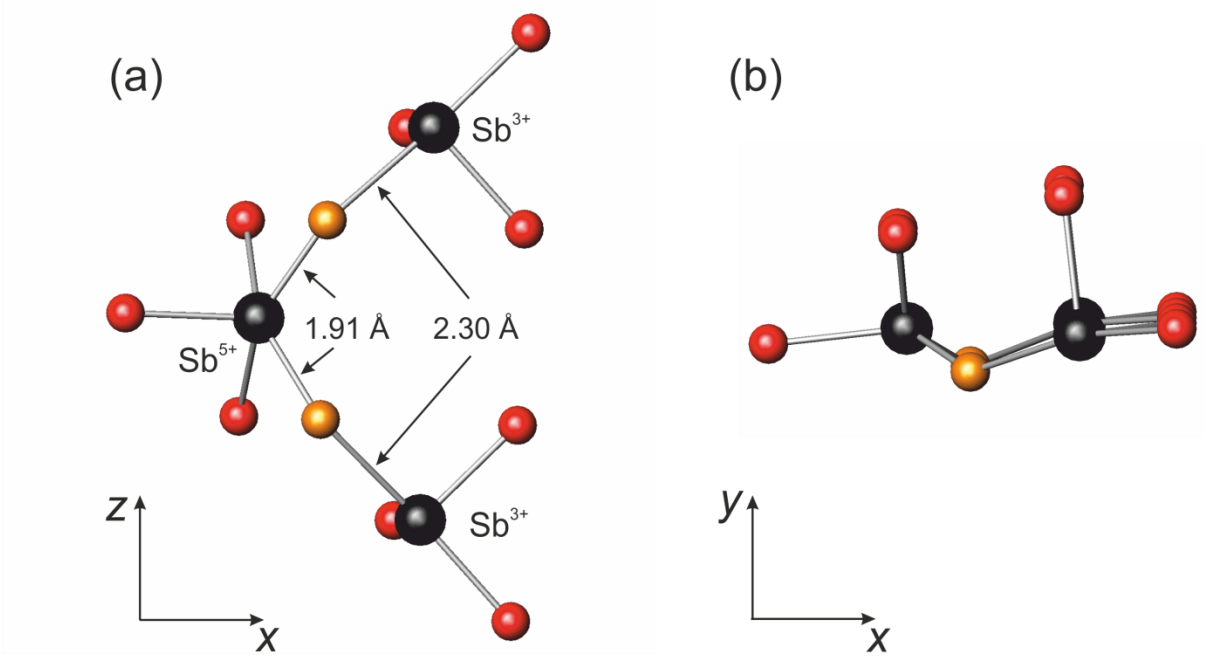

Fig.17

For Table of Contents Only

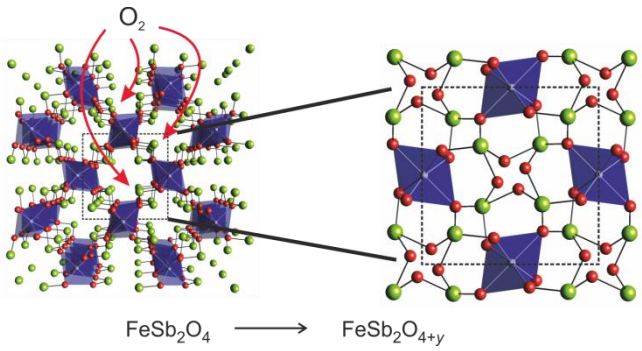

$FeSb_2O_4$ and related phases contain chains of edge-linked FeO_6 octahedra separated Sb^{3+} ions which form the walls of empty channels. For phases that contain both Fe^{2+} and Sb^{3+} it is shown that low-temperature oxidation occurs to form non-stoichiometric oxygen-excess materials. Using a range of structural and spectroscopic methods, have demonstrated that the oxidation involves the incorporation of oxide ions within the channels and oxidation of both Fe^{2+} to Fe^{3+} and Sb^{3+} to Sb^{5+}.